Acta Pharmaceutica Sinica B 2024;14(8):3643−3660

Chinese Pharmaceutical Association
Institute of Materia Medica, Chinese Academy of Medical Sciences

Acta Pharmaceutica Sinica B

www.elsevier.com/locate/apsb
www.sciencedirect.com

ORIGINAL ARTICLE

Endoplasmic reticulum-targeted delivery of celastrol and PD-L1 siRNA for reinforcing immunogenic cell death and potentiating cancer immunotherapy

Jie Wang[a,b,†], Zilong Zhang[a,b,†], Yan Zhuo[b,c], Zhuan Zhang[d], Rongrong Chen[d], Li Liang[d], Xiaohe Jiang[b,e], Di Nie[b], Chang Liu[b,e], Zhiwen Zou[b], Xiang Li[b,e], Jiaxin Li[b,e], Bingqi Wang[b,e], Rui Wang[a,*], Yong Gan[b,d,e,f,*], Miaorong Yu[b,e,*]

[a]*School of Pharmacy, Shanghai University of Traditional Chinese Medicine, Shanghai 201203, China*
[b]*State Key Laboratory of Drug Research, Shanghai Institute of Materia Medica, Chinese Academy of Sciences, Shanghai 201203, China*
[c]*Jiangxi Medical College, Nanchang University, Nanchang 330006, China*
[d]*School of Pharmacy, Nanjing University of Chinese Medicine, Nanjing 210023, China*
[e]*University of Chinese Academy of Sciences, Beijing 100049, China*
[f]*NMPA Key Laboratory for Quality Research and Evaluation of Pharmaceutical Excipients, National Institutes for Food and Drug Control, Beijing 100050, China*

Received 4 February 2024; received in revised form 4 March 2024; accepted 13 March 2024

KEY WORDS

Chemoimmunotherapy;
Targeted drug delivery;
Endoplasmic reticulum;
Endoplasmic reticulum stress;
Immunogenic cell death;
siRNA;

Abstract The prospect of employing chemoimmunotherapy targeted towards the endoplasmic reticulum (ER) presents an opportunity to amplify the synergistic effects of chemotherapy and immunotherapy. In this study, we initially validated celastrol (CEL) as an inducer of immunogenic cell death (ICD) by promoting ER stress and autophagy in colorectal cancer (CRC) cells. Subsequently, an ER-targeted strategy was posited, involving the codelivery of CEL with PD-L1 small interfering RNAs (siRNA) using KDEL peptide-modified exosomes derived from milk (KME), to enhance chemoimmunotherapy outcomes. Our findings demonstrate the efficient transportation of KME to the ER *via* the Golgi-to-ER pathway. Compared to their non-targeting counterparts, KME exhibited a

*Corresponding authors.
E-mail addresses: ellewang@163.com (Rui Wang), ygan@simm.ac.cn (Yong Gan), mryu@simm.ac.cn (Miaorong Yu).
[†]These authors made equal contributions to this work.

Peer review under the responsibility of Chinese Pharmaceutical Association and Institute of Materia Medica, Chinese Academy of Medical Sciences.

https://doi.org/10.1016/j.apsb.2024.04.010

Exosomes;
Colorectal cancer

significant augmentation of the CEL-induced ICD effect. Additionally, it facilitated the release of danger signaling molecules (DAMPs), thereby stimulating the antigen-presenting function of dendritic cells and promoting the infiltration of T cells into the tumor. Concurrently, the ER-targeted delivery of PD-L1 siRNA resulted in the downregulation of both intracellular and membrane PD-L1 protein expression, consequently fostering the proliferation and activity of $CD8^+$ T cells. Ultimately, the ER-targeted formulation exhibited enhanced anti-tumor efficacy and provoked anti-tumor immune responses against orthotopic colorectal tumors *in vivo*. Collectively, a robust ER-targeted delivery strategy provides an encouraging approach for achieving potent cancer chemoimmunotherapy.

1. Introduction

Chemoimmunotherapy has emerged as a groundbreaking approach in cancer treatment, combining traditional chemotherapy with immunotherapy to enhance the body's natural immune response against cancer cells[1-4]. One notable advancement in this field involves the integration of chemotherapeutics with programmed death-ligand 1 small interfering RNA (PD-L1 siRNA)[5-8]. Chemotherapy works by directly targeting and killing rapidly dividing cancer cells, while PD-L1 siRNA addresses the immune evasion mechanism employed by tumors. By suppressing both the cell membrane and intracellular PD-L1 expression, the treatment enhances the immune system's ability to recognize and attack cancer cells[9-10]. This combined strategy not only delivers a direct assault on tumor cells but also potentiates the intrinsic defense mechanisms of the body, resulting in a more comprehensive and synergistic therapeutic effect with the potential to enhance treatment efficacy[11]. Currently, numerous systems have been devised to enhance the therapeutic efficacy of chemoimmunotherapy and minimize adverse effects through tumor-targeted delivery. However, given that the targets of these therapeutics are typically intracellular, the optimization of chemoimmunotherapy necessitates addressing pertinent challenges, particularly the precise intracellular targeting of both chemotherapeutics and PD-L1 siRNA. The efficient and targeted delivery of therapeutic agents into intracellular targets remains a formidable obstacle, and the potential compromise of therapeutic efficacy due to nonspecific intracellular distribution underscores the critical importance of addressing this limitation.

The endoplasmic reticulum (ER) assumes a pivotal intracellular role in the context of chemoimmunotherapy due to its central involvement in cellular processes and its capacity to induce immunogenic cell death (ICD)[12-14]. ER stress, precipitated by diverse cellular perturbations, activates pathways leading to ICD, an immunostimulatory form of cell death eliciting an immune response against cancer cells[15-17]. The ICD-inducing approach not only promotes the release of damage-associated molecular patterns (DAMPs) but also augments the tumor infiltration of T cells, countering the immunosuppressive tactics employed by tumors[18-19]. Crucially, the ER serves as a central nucleation site of siRNA-mediated RNA silencing[20], and the synthesis site for proteins such as PD-L1, a pivotal immune checkpoint molecule[21]. Targeting the ER in chemoimmunotherapy provides a dual advantage, wherein chemotherapeutics induce ER stress, promoting ICD and facilitating the release of tumor-associated antigens. Concurrently, inhibition of PD-L1 synthesis within the ER disrupts tumor immune evasion mechanisms. This integrative approach capitalizes on the interconnected nature of ER stress, ICD, and PD-L1 synthesis, potentially amplifying the overall anti-cancer immune response. Thus, the exploration of ER-targeting in chemoimmunotherapy holds promise for maximizing therapeutic benefits, an avenue that has been relatively underexplored in current research endeavors.

In this study, colorectal cancer was chosen as the disease model due to its high incidence and mortality, as well as the resistance of colorectal cancer to immunotherapy. We first verified the capacity of celastrol (CEL) to induce ICD by promoting ER stress and autophagy in CRC cells. We then proposed an ER-targeted strategy, delivering CEL with PD-L1 siRNA using KDEL peptide-modified exosomes derived from milk (KME), to boost chemoimmunotherapy. Compared to non-targeting counterparts, KME exhibited superior cellular uptake, intracellular trafficking, and distribution, particularly in the ER. CEL-loaded KME then contributed to an amplified ICD effect, resulting in increased cytotoxicity, apoptosis, the release of DAMPs, and the maturation of dendritic cells (DCs). Meanwhile, siRNA released in the ER would substantially down-regulate both intracellular and membrane PD-L1 protein expression. Accordingly, the combination of CEL and PD-L1 siRNA within KME (KME@CEL+siPD-L1) synergistically promotes T cell proliferation and cytotoxic activity, significantly surpassing the mono drug group. In an orthotopic CRC mouse model, orally administrated KME@CEL+siPD-L1 demonstrated a significant reduction in tumor growth, prolonged overall survival, and minimal systemic toxicity compared with the non-targeting group. Notably, KME@CEL+siPD-L1 induced a robust immunological response, characterized by increased exposure of calreticulin (CRT), downregulation of PD-L1, maturation of dendritic cells (DCs), and enhanced infiltration of $CD8^+$ T cells into the tumor microenvironment. In conclusion, this study introduces an innovative chemoimmunotherapeutic approach for CRC, leveraging the synergistic effects of CEL-induced ICD and PD-L1 siRNA-mediated immune modulation. The use of ER-targeted exosomes enhances the delivery and effectiveness of this combination strategy, offering a promising avenue for advancing cancer treatment strategies.

2. Materials and methods

2.1. Materials

Fresh bovine milk was purchased from Bright Dairy & Food Co., Ltd. KDEL peptide was obtained from Hefei Sen'er Biotechnology

Co., Ltd. (Hefei, China). Negative siRNA, Cy3-labeled siRNA, and PD-L1 siRNA were purchased from Shanghai GenePharma Co., Ltd. (Shanghai, China). Celastrol, Lipofectamine 2000 (Lipo2000), fetal bovine serum (FBS) and Dulbecco's modified Eagle's medium (DMEM) were bought from Thermo Fisher Scientific Inc. (Waltham, USA). Simulated gastric fluid (SGF), simulated intestinal fluid (SIF), and simulated colonic fluid (SCF) were bought from Shanghai Yuanye Bio-Technology Co., Ltd. (Shanghai, China). The fluorescent dyes of 1,1′-dioctadecyl-3,3,3′,3′-tetramethylindocarbocyanine perchlorate (DiI), carbocyanine (DiD) and 2-(4-aminophenyl)-6-indolecarbamidine dihydrochloride (DAPI), the radioimmunoprecipitation assay (RIPA) buffer, protease inhibitor cocktail, Lyso-Tracker Green, D-luciferin potassium and bicinchoninic acid (BCA) protein assay kit were obtained from Dalian Meilun Biotechnology Co., Ltd. (Dalian, China). Annexin V-FITC/PI apoptosis detection kit and Alexa Fluor 647 labeled goat anti-mouse secondary antibody were purchased from Yeasen Biotechnology Co., Ltd. (Shanghai, China). ER-Tracker Green and Golgi-Tracker Green were obtained from Beyotime Inc. (Shanghai, China). APC anti-CD11c, PE anti-CD86, FITC anti-CD80, APC anti-CD3, FITC anti-CD4, PE anti-CD8, and PE anti-CD274 were purchased from BioLegend Inc. (San Diego, USA). Mouse TNF-α and IL-6 ELISA kits were purchased from Shanghai Jingkang Bioengineering Co., Ltd. (Shanghai, China). All other reagents were bought from Sinopharm Chemical Reagent Co., Ltd. (Shanghai, China).

2.2. Cell culture

Mouse colon cancer cells (CT26 cells and CT26-Luc cells) and human colorectal adenocarcinoma cells (Caco-2 cells) were cultured in DMEM with 1% penicillin−streptomycin supplementation and 10% FBS. Mucus-secreted human colorectal cells (HT29-MTX cells) were cultured in McCOY's 5A medium with 1% penicillin−streptomycin supplementation and 10% FBS. Human normal colonic epithelial cells (NCM460 cells) were cultured in RPMI1640 medium with 1% penicillin−streptomycin supplementation and 10% FBS.

Bone-marrow-derived dendritic cells (BMDCs) were harvested from BALB/c mice. Bones were isolated and cut using needles to flush out marrow cells with an isolation medium. The cells were resuspended and cultured in a 6-well plate (2×10^6/well) with 2 mL of complete RPMI-1640 medium. Each well was supplemented with 20 ng/mL GM-CSF and 10 ng/mL IL-4. Every 2 days, the supernatant was replaced with fresh medium containing GM-CSF and IL-4. On Day 5, suspended and loosely adherent cells were harvested as immature BMDCs for the following experiments. Splenic lymphocytes were extracted from BALB/c mice at 8 weeks of age using Mouse 1 × Lymphocyte Separation Medium (Dakewei Biotech Co., Ltd., Shanghai, China).

2.3. Animals

Female BALB/c mice, aged 6 weeks and weighing between 18 and 22 g, were obtained from the Animal Experiment Center at the Shanghai Institute of Materia Medica in China. The execution of all animal experiments adhered strictly to the guidelines set forth by the Institutional Animal Care, under the supervision of the Animal Ethics Committee of SIMM (IACUC code: 2022-10-GY-66).

2.4. Isolation of milk-derived exosomes

Fresh milk underwent centrifugation at $3000\times g$ to separate cells and cellular debris. The resulting defatted samples were then mixed with 50 mmol/L EDTA at 37 °C to facilitate chelation of the casein−calcium complex[22]. Subsequently, the mixture underwent sequential centrifugation at $2000\times g$ and $12{,}000\times g$ for 1 h, respectively. The resulting supernatant was concentrated to a reduced volume using a tangential flow device and subsequently subjected to centrifugation at $160{,}000\times g$ to precipitate milk-derived exosomes (ME). Following this, the ME underwent a purification regimen that capitalized on an iodixanol gradient of differential concentrations to enhance the purification efficacy. Fractions distinguished by iodixanol concentrations within the 20%−40% bracket were subsequently collected, diluted in phosphate-buffered saline (PBS), and subjected to centrifugation, culminating in the successful isolation of purified ME[23-24]. The isolated ME was then preserved at −80 °C. The protein amount of ME was measured *via* BCA kits.

2.5. Synthesis of DSPE-KDEL

A cysteine residue of KDEL was covalently bound with the maleimide group of DSPE-PEG_{2000} through a Michael-type addition reaction. In brief, DSPE-PEG_{2000} and KDEL peptide were dissolved in 4 mL of *N*,*N*-dimethylformamide (DMF) and stirred overnight. Subsequently, the resulting solution was purified by dialysis (molecular weight cutoff: 10 kDa) against deionized water and then lyophilized to yield the DSPE-PEG_{2000}-KDEL. Proton Nuclear Magnetic Resonance (^{1}H NMR) and Fourier Transform Infrared Spectrometer (FTIR) were used to confirm the structure of DSPE-PEG_{2000}-KDEL.

2.6. Preparation and characterization of KME

The ME and DSPE-KDEL were mixed at a weight ratio of 15:1 and incubated at 37 °C for 4 h. Subsequently, the mixture was centrifuged to precipitate KME. The obtained KME pellet was resuspended and stored at −80 °C. Exosome morphology was observed by transmission electron microscopy (TEM, Tecnai G2 Spirit, FER, USA) with an acceleration voltage of 120 kV. The size and zeta potential were measured using a Zetasizer (Nano ZS, Malvern Instruments, UK). The fluorescence colocalization between FITC-labeled DSPE-KDEL and DiI-labeled exosomes was visualized using stimulated emission depletion (STED) microscopy. Additionally, the distinctive proteins inherent in exosomes were identified through Western blot analysis, including TSG101, CD63, and calnexin. For exosomes stability studies, exosomes were mixed (1:10, *v*/*v*) and incubated with PBS for 2 h, simulated gastric fluid (SGF) for 2 h, simulated intestinal fluid (SIF) for 4 h and simulated colonic fluid (SCF) for 8 h. At the predetermined time intervals, samples were taken out to measure the size and polydispersity indexes (PDI) of the exosomes.

2.7. Preparation and characterization of exosomes coloaded with CEL and siRNA

The PD-L1 siRNA was introduced into exosomes (1:20, *w*/*w*) *via* electroporation in a citric acid-based buffer (pH 4.4) using 2 mm cuvettes with parameters set at 400 V and 125 μF, which obtained PD-

L1 siRNA-loaded exosomes (ME@siPD-L1 and KME@siPD-L1). Subsequently, the exosomes were mixed with CEL (20:1, *w*/*w*) and stirred at 4 °C for 24 h. The solution was centrifugated at 10,000×*g* for 10 min to precipitate unencapsulated CEL, and further centrifugated at 160,000×*g* to obtain CEL and siRNA coloaded exosomes (ME@CEL+siPD-L1 and KME@CEL+siPD-L1).

The encapsulation efficiency (EE%) and loading capacity (LC %) of CEL were determined by high-performance liquid chromatography (HPLC). The EE (%) and LC (%) of siRNA were assessed using a microplate reader, with an excitation wavelength at 550 nm and an emission wavelength at 570 nm. Calculations for both EE and LC were conducted as shown in Eqs. (1) and (2):

$$\mathrm{EE}\,(\%) = \frac{\text{Weight of encapsulated drug}}{\text{Weight of added drug}} \times 100 \quad (1)$$

$$\mathrm{LC}\,(\%) = \frac{\text{Weight of encapsulated drugs}}{\text{Weight of exosome and encapsulated drugs}} \times 100 \quad (2)$$

The *in vitro* release of KME@CEL and ME@CEL was studied using pH 6.8 PBS. First, KME@CEL and ME@CEL were placed in PBS (pH = 6.8) for 144 h. During the process, 500 μL samples were taken at 0, 1, 2, 4, 6, 8, 12, 24, 48, 72, 96, 120, and 144 h, and 500 μL of the same medium was supplemented. The content of CEL was determined by HPLC at 452 nm and the cumulative CEL release was calculated.

To examine the resistance of siRNA-loaded exosomes against nuclease-mediated degradation and acid environment of the stomach, the siRNA NPs were incubated with RNase (50 U/mL) or SGF at 37 °C for 0, 0.5, 1, and 2 h. At the predetermined time intervals, the integrity of siRNA was examined by electrophoresis. Free siRNA was used as a control.

2.8. *Induction of immunogenic cell death (ICD) by CEL and amplification of ICD effect via ER target*

The *in vitro* cytotoxicity of CEL, ME@CEL, and KME@CEL was evaluated using a Cell Counting Kit-8 (CCK-8) cell proliferation assay, following a modified manufacturer's protocol. CT26 cells were cultured in 96-well plates for 24 h, and the subsequent treatments at predetermined concentrations were added. After an additional 24-h incubation, the culture medium was replaced with 10% CCK-8 reagent, and plates were incubated at 37 °C for 15 min. Absorbance at 450 nm was measured with each sample concentration tested in triplicate, and three independent experiments were conducted.

The *in vitro* apoptosis was assessed using flow cytometry (Becton Dickinson, Fortessa, NJ, USA). CT26 cells were plated in 24-well plates and allowed to incubate for 24 h. Subsequently, CEL, ME@CEL, and KME@CEL were added and incubated with CT26 cells for an additional 24 h. After incubation, apoptosis analysis was executed using an Annexin V-FITC/PI apoptosis detection kit in conjunction with flow cytometry. Data analysis was carried out using Flow Jo (version 10).

The activity of protein kinase RNA-like endoplasmic reticulum kinase (PERK) signaling pathways was examined using a Western blotting assay. CT26 cells were cultured in 12-well plates for 24 h, treated with CEL, ME@CEL, and KME@CEL at their specific concentrations, and incubated for an additional 24 h. The total protein content was quantified using the BCA Protein Assay kit and then separated by a 4%−20% SDS-PAGE gel. The samples were subsequently transferred to a PVDF membrane through electrophoretic blotting. The PVDF membranes were blocked and incubated with antibodies against anti-PERK, anti-p-PERK, anti-Caspase-3, anti-c-Caspase-3, anti-c-Caspase-9, anti-LC3-I, anti-LC3-II, and anti-GAPDH (Wanleibio Co., Ltd., Shenyang, China). The horseradish peroxidase (HRP)-conjugated goat anti-rabbit antibodies served as the secondary antibody, and the analysis was performed using an automatic chemiluminescence imaging system. Meanwhile, the quantitative analysis of the LC3-II/LC3-I ratio according to Western blot bands was conducted by ImageJ.

The exposure of CRT was detected using an immunofluorescent staining assay. CT26 cells were seeded onto cell-attached slides in a 24-well plate and treated with CEL, ME@CEL, and KME@CEL for 4 h. Cells were fixed in 4% paraformaldehyde, blocked, incubated with mouse anti-CRT antibody (Santa Cruz Biotechnology, Inc., Dallas, USA) overnight, and exposed to Alexa Fluor 647 label-goat anti-mouse secondary antibody. After stained with DAPI, cells were analyzed using confocal laser scanning microscopy (CLSM).

The secretion of adenosine triphosphate (ATP) and release of HMGB1 were assessed using bioluminescent and enzyme-linked immunosorbent assay (ELISA) assays. CT26 cells were seeded in a 6-well plate and treated with CEL, ME@CEL, and KME@CEL at specified concentrations for 12 and 24 h, respectively. The ATP content in the supernatant was determined using an ATP assay kit (Shanghai Xuyu Biotechnology Co., Ltd.) following the provided instructions, and the level of HMGB1 in the supernatant was quantified with an HMGB1 ELISA kit (Shanghai Acmec Biochemical Co., Ltd.).

The maturation of BMDCs was determined using flow cytometry (Becton Dickinson). BMDCs and CT26 cells were separately seeded in 12-well plates. CT26 cells were treated with CEL, ME@CEL, and KME@CEL (with CEL concentration of 2.5 μmol/L) for 24 h. The resulting supernatant medium, containing tumor-released antigens such as HMGB1 and ATP, was collected and exposed to BMDCs for 48 h. Cells were stained with anti-CD86 (PE), anti-CD11c (APC), and anti-CD80 (FITC) antibodies, and then analyzed using flow cytometry and Flow Jo.

The *in vivo* vaccination assay was performed as previously described[25]. Briefly, 3×10^6 CT26 cells, severally treated with PBS, free CEL, ME@CEL, and KME@CEL for 12 h, were s.c. implanted into the right flank of BALB/c mice ($n = 8$ mice per group). One week later, 3×10^5 CT26 cells were s.c. implanted into the left flank. Tumor development in the left flank was monitored to determine tumor-free mice.

2.9. *Cellular uptake*

CT26 cells (1×10^5 per well) were seeded onto cell-attached slides in a 24-well plate and incubated with DiI-labeled exosomes (ME and KME with protein concentration of 100 μg/mL), Cy3-labeled siRNA-loaded formulations (Free Cy3 siRNA, ME@Cy3 siRNA, KME@Cy3 siRNA, and Lipo2000@Cy3 siRNA with an siRNA concentration of 150 nmol/L), respectively. After a 2-h incubation, the cells were fixed and stained for CLSM analysis.

The quantification of cellular uptake of exosomes and siRNA-loaded formulations was performed using flow cytometry. CT26 cells were seeded in a 24-well plate and incubated for 24 h, followed by a 2-h incubation with the formulations above. After three washes with PBS, the fluorescent intensity was quantified using flow cytometry. Data analysis was conducted using Flow Jo (version 10).

2.10. Intracellular trafficking pathways

To investigate intracellular trafficking pathways, CT26 cells were exposed to DiI-labeled exosomes or Cy3 siRNA-loaded formulations and incubated for 4 h. Subsequently, the cells were stained with Hoechst 33342 and specific organelle dyes (Lyso-Tracker Green, ER-Tracker Green or Golgi-Tracker Green). Colocalization signals of exosomes or Cy3 siRNA with organelles were visualized using CLSM. Similar experiments were conducted when CT26 cells were pre-treated with the Golgi inhibitor Golgicide A (GCA, 10 μmol/L) to explore the role of coat protein complex I (COPI) vesicles in the transport pathway of KME. The degree of colocalization was analyzed using ImageJ software.

Furthermore, CT26 cells (1×10^5 per well) were incubated with DiI-labeled ME and KME. Following a 4-h incubation, the cells were fixed in 4% paraformaldehyde, blocked, and incubated overnight with rabbit anti-COPI antibody (ABclonal Biotech Co., Ltd., Wuhan, China). Subsequently, an Alexa Fluor 647 label-goat anti-rabbit secondary antibody was applied, and the cells were imaged using CLSM after being stained with DAPI.

2.11. In vitro gene silencing effects

To assess the relative expression level of PD-L1 mRNA, the cells treated with different formulations were analyzed by real-time quantitative polymerase chain reaction (RT-qPCR) assay. CT26 cells (2×10^5 cells per well) were seeded into 12-well plates. After 24-h proliferation, various formulations (CEL+siPD-L1, KME@CEL, KME@siPD-L1, ME@CEL+siPD-L1, and KME@CEL+siPD-L1) were incubated with CT26 cells for 48 h, with a final concentration of PD-L1 siRNA at 150 nmol/L and CEL at 2.5 μmol/L. Total RNAs from the treated CT26 cells were extracted using the Trizol Reagent Kit. Reverse transcription of mRNA and RT-qPCR experiments were conducted using the PrimeScript™ RT reagent Kit with gDNA Eraser and TB Green™ Premix Ex Taq™, respectively. The mRNA expression levels were quantified using the Applied Biosystems 7500 Fast Real-Time PCR System (ABI, USA) and calculated using the $2^{-\Delta\Delta Ct}$ (threshold cycle) method. For PD-L1, the forward primer was designed as 5′-GCTCCAAAGGACTTGTACGTG-3′ and the reverse primer was designed as 5′-TGATCTGAAGGGCAGCATTTC-3′; for GAPDH, the forward primer was designed as 5′-TCAACAGCAACTCCCACTCTTCCA-3′ and the reverse primer was designed as 5′-ACCCTGTTGCTGTAGCCGTATTCA-3′.

For flow cytometry investigation of PD-L1 protein expression levels, CT26 cells were seeded into 12-well plates and incubated with the aforementioned formulations. After 48 h of incubation, CT26 cells were stained with PE anti-CD274 and analyzed using flow cytometry.

For Western blotting analysis of PD-L1 protein expression levels, similar cell cultures and treatments were performed as described above. After 48 h of incubation, the cells were washed with pre-cooled PBS and then re-suspended in 100 μL RIPA lysis buffer supplemented with a 1% proteinase inhibitor cocktail. The total protein concentration was determined with the BCA Protein Assay Kit. Total protein (30 μg) was loaded on a 12% SDS-polyacrylamide gel and electrophoresed for 1 h. The proteins were then transferred to PVDF membranes at 400 mA for 20 min and blocked with 5% skimmed milk for 1 h. The membranes were incubated with the anti-PD-L1 monoclonal antibody (Wanleibio Co., Ltd., Shenyang, China) overnight at 4 °C followed by the incubation with HRP-conjugated goat anti-rabbit antibodies at room temperature. Finally, the membranes were exposed using a Bio-rad ChemiDoc XRS System, with GAPDH utilized as an endogenous control.

For the immunofluorescent staining assay of PD-L1 protein expression levels, similar cell cultures and treatments were performed as described above. After 48 h of incubation, the cells were fixed in 4% paraformaldehyde, blocked, and incubated with rabbit anti-PD-L1 antibody overnight and Alexa Fluor 647 label-goat anti-rabbit secondary antibody. After being stained with DAPI, cells were imaged using CLSM. The degree of colocalization was analyzed using ImageJ software.

2.12. In vitro T cell proliferation

CT26 cells (4×10^4 cells per well) were seeded in 6-well plates. Various formulations were added and incubated with CT26 cells for 24 h. Subsequently, BMDCs (2×10^5 cells per well) were introduced and cocultured with CT26 cells for another 24 h. The spleen lymphocytes were isolated from BALB/c mice through density gradient centrifugation and added to the pre-treated mixed cells at 8×10^4 cells per well to construct a tumor-BMDCs-T cell coculture system. Three days later, T cells in the medium were collected, stained with APC anti-CD3 and PE anti-CD8 antibodies, and then analyzed by flow cytometry.

2.13. In vitro biocompatibility of KME@CEL+siPD-L1 on normal cells

NCM460 cells were cultured in 96-well plates for 24 h, and the subsequent treatments at predetermined concentrations of CEL, ME@CEL, and KME@CEL were added. After an additional 24-h incubation, the culture medium was replaced with 10% CCK-8 reagent, and plates were incubated at 37 °C for 15 min. Absorbance at 450 nm was measured with each sample concentration tested in triplicate, and three independent experiments were conducted.

The quantification of cellular uptake of KME was performed using flow cytometry. CT26 cells and NCM460 cells were seeded in a 24-well plate and incubated for 24 h, followed by a 2-h incubation with the high (100 μg/mL) and low (40 μg/mL) concentration of DiI-labeled KME. After three washes with PBS, the fluorescent intensity was quantified using flow cytometry. Data analysis was conducted using Flow Jo (version 10).

2.14. Absorption studies across the mucus and epithelium

The experiment was conducted as published procedures with slight modifications[26]. To observe mucus penetration in three dimensions, the mouse colon was ligated with medical sutures. After staining the mucus with Alexa Fluor 488-conjugated-wheat germ agglutinin (WGA) for 10 min, 100 μL of DiI-labeled ME and KME were slowly injected and incubated for an additional 30 min, respectively. The intestinal segment was then excised, and a z-stack model was employed to visualize the mucus penetration property in a 3D pattern.

The transepithelial transport of exosomes was studied using a Caco-2 cell monolayer on a Transwell chamber. Inserts with transepithelial electrical resistance (TEER) values ranging from 1000 to 1200 $\Omega \times cm^2$ were selected for the subsequent experiments. The transepithelial efficiency was assessed by introducing DiI-labeled ME, KME, and PEGylated liposomes into the apical chamber, while the basolateral chamber contained an HBSS solution. At different time points (0, 1, 2, 3, 4, 6, and 8 h), the

medium from the basolateral chamber was collected for fluorescent intensity measurement, with an equal volume of fresh medium simultaneously added.

To explore the integrity of exosomes transported across Caco-2 cells, the double fluorophores-labeled nanoparticles (FAM-labeled siRNA-loaded DiI-labeled ME and KME) were prepared through electroporation and introduced into the apical chamber of the Transwell system. After 8-h incubation, the basolateral medium was collected, and Förster resonance energy transfer (FRET) emission was measured on a microplate reader with excitation at 450 nm.

To explore the transepithelial transport mechanism, the Caco-2 cell monolayer preincubated with DiI-labeled ME, KME, and PEGylated liposomes were labeled with the neonatal Fc receptor (FcRn) mouse monoclonal antibody (Santa Cruz Biotechnology, Inc., Dallas, USA) and anti-mouse IgG Alexa Fluor 647 secondary antibody. The colocalization results were captured by CLSM, and the quantitative analysis was performed using ImageJ software.

For assessing the anticancer effect after transepithelial transport, mixed Caco-2 and HT29-MTX (7:3) cells were seeded in a Transwell apical chamber (24-well, 0.4 μm; Corning). When the TEER value exceeded 300 Ω/cm^2, CT26 cells were seeded in the basal chamber and incubated for 12 h. Free CEL and PD-L1 siRNA, ME@CEL+siPD-L1, and KME@CEL+siPD-L1, with CEL and PD-L1 siRNA concentrations of 2.5 μmol/L and 150 nmol/L, respectively, were added into the apical chamber and incubated for 30 h. Subsequently, CT26 cells were stained using an Annexin V-FITC/PI apoptosis detection kit, and the cells were analyzed by CLSM.

2.15. Mouse orthotopic colorectal cancer model

BALB/c mice were secured in the supine position and anesthetized. The cecum was carefully exteriorized, and approximately 1×10^6 CT26-Luc cells were administrated to the cecal wall using an insulin-gauge syringe. After tumor inoculation (Day 0), mice received intraperitoneal injections (i.p.) of 100 μL luciferin (30 mg/mL; Pierce), and tumor development was consistently monitored using an IVIS Kinetics Optical System (PerkinElmer). Tissue distribution and pharmacodynamics studies were performed when luminescence intensities reached approximately 1×10^6 photons (p)/s/cm^2/sr on Day 10.

2.16. Tumor accumulation studies

The tumor-bearing mice were orally administered with free DiR dye and DiR-labeled ME and KME. At the time points of 2, 6, and 12 h, the living images were obtained using an IVIS *in vivo* system (748/780 nm) to capture the exosome distribution in the intestine. After 12 h, the mice were sacrificed, and the colon along with major organs (heart, liver, spleen, lungs, and kidneys) were harvested. The fluorescence intensity of DiR in the organs was assessed after rinsing with PBS.

2.17. Colocalization with organelles in tumor tissues

To measure the intracellular locations of KME and ME *in vivo*, the tumor tissues were obtained from the mice at 12 h postinjection after intragastric administrating the DiD-labeled ME and KME to mice, and then sliced and observed by immunofluorescence staining. The tumor sections were fixed, blocked, and incubated with LAMP1 rabbit mAb, Golgin-97 (CDF4) mouse mAb, or calregulin mouse mAb (Abcam Co., Cambridge, UK) overnight and corresponding secondary antibody to label lysosome, Golgi, and ER. After stained nuclei with DAPI, images were captured using CLSM.

2.18. In vivo antitumor efficacy

The tumor-bearing mice were randomly divided into five groups ($n = 5$) and received intragastric administration of saline, KME@siPD-L1, KME@CEL, ME@ CEL+siPD-L1, and KME@CEL+siPD-L1 at siRNA dose of 0.1 mg/kg and CEL dose of 3 mg/kg every 2 days for 3 weeks. The body weight of the mice was recorded every 5 days. Furthermore, the mice in each group received intraperitoneal injections of D-luciferin (150 mg/kg) every 7 days; then, the mice were anesthetized and imaged to monitor the tumor bioluminescence following our previously reported method[27]. At the end of the treatment, the mice were euthanized, and their tumors, intestines, and major organs (heart, liver, spleen, lung, and kidneys) were collected for histological examination. The blood samples were collected and analyzed for the serum cytokines of alanine transaminase (ALT) and aspartate transaminase (AST), blood urea nitrogen (BUN), and creatinine (CRE). And tumor necrosis factor-alpha (TNF-α) and interleukin-6 (IL-6), were measured using the corresponding ELISA kits according to the manufacturer's protocols.

2.19. In vivo antitumor immunity

To investigate the antitumor immune function within tumor tissues, the tumors were isolated and sectioned following different treatments. Subsequently, the tumor tissues were incubated with an anti-CRT antibody or anti-PD-L1 antibody and stained with DAPI. After sealing, the fluorescence images were captured using CLSM.

Furthermore, the spleens, mesenteric lymph nodes, and tumors were isolated. Organs were finely minced using surgical scissors and then passed through a 70 μm filter. After the majority of red blood cells were lysed, the cells were collected as single-cell suspensions. The spleen cells and tumor cells were stained with fluorescence-labeled antibodies CD3, CD4, and CD8, while the lymphocytes were stained with fluorescence-labeled antibodies CD11c, CD80, and CD86 for 20 min. All samples were evaluated by flow cytometry and analyzed with FlowJo software.

2.20. Statistical analysis

All the experimental data were collected in triplicate, unless explicitly stated otherwise, and were presented as the mean ± standard deviation (SD). One-way analysis of variance (ANOVA) was employed for comparisons among multiple groups, while Student's *t*-test was utilized for comparisons between two groups. Significance levels were determined based on P values ($^*P < 0.05$; $^{**}P < 0.01$; $^{***}P < 0.001$; and $^{****}P < 0.0001$).

3. Results and discussion

3.1. CEL-induced ICD in CRC cells by promoting ER stress and autophagy

Celastrol (CEL), derived from *Tripterygium wilfordii* roots, is acknowledged for its potential to induce ICD by promoting ER stress and autophagy[28-30]. Despite its recognized potential, CEL's specific ICD-inducing capability in CRC cells remains elusive. Using the CT26 cell model, we first revealed that CEL induced

CT26 cell apoptosis in a concentration-dependent manner, with an IC_{50} value of 2.5 μmol/L (Supporting Information Fig. S1A–S1C). Further investigations into CEL's potential as an ICD inducer demonstrated its ability to activate the PKR-like ER kinase (PERK) pathway. Specifically, CEL induced PERK phosphorylation (p-PERK) while decreasing PERK expression (Fig. S1D), concurrently upregulating downstream proteins c-caspase 9 and c-caspase 3 (Fig. S1D), indicative of ER stress. The transition from light chain 3-I (LC3-I) to light chain 3-II (LC3-II), a crucial marker for autophagy, was substantially increased post-treatment, as evidenced by a heightened LC3-II/LC3-I ratio (Fig. S1D). Additionally, CEL induced characteristic DAMPs[31], including increased calreticulin (CRT) exposure, extracellular ATP, and high mobility group box 1 (HMGB1) release in CT26 cells (Fig. S1E–S1G). This evidence demonstrated that CEL effectively triggered both ER stress and autophagy, facilitating ICD.

It is reported that the released DAMPs play a crucial role in antigen-presenting cells (APCs) recognition[32]. The *in vitro* analysis by counting mature BMDCs ($CD11c^+CD86^+$, mDCs) showed that CEL-induced mDCs significantly increased, reaching 39.0%, as opposed to the control's 1.1% (Fig. S1H and S1I). Altogether, these findings underscored CEL's potential not only in inducing ER stress and autophagy-associated ICD in CRC cells but also in promoting DCs maturation, highlighting CEL as a promising ICD inducer against CRC.

3.2. Preparation and characterization of ER-targeted exosomes

Milk-derived exosomes (ME) have been widely accepted as promising carriers to transport diverse biomolecules and chemotherapeutic agents[33-34], with good stability and low immunogenicity, showing excellent cross-species tolerance[35]. Herein, we used ME to fabricate the ER-targeted drug delivery system. The incorporation of peptides possessing KDEL sequences at their terminals, known to bind with the KDEL receptor present in the Golgi and ER, facilitates ER retention[36-37]. To confer ER-targeting ability onto ME, DSPE-PEG_{2000}-KDEL was synthesized by utilizing the cysteine residue on KDEL peptide to link DSPE-PEG_{2000}-Mal. Successful synthesis was confirmed through the disappearance of the double bond hydrogen signal at 6.6 ppm in the nuclear magnetic hydrogen spectrum (^{1}H NMR) and the appearance of the thioether bond at 1200 cm^{-1} in the infrared spectrum (Supporting Information Fig. S2). Subsequently, 50 mg purified ME was yielded from 1 L of fresh milk[23], which was further modified with DSPE-PEG_{2000}-KDEL using the post-insertion technique to obtain ER-targeted ME (KME).

The morphological characteristics of ME and KME were elucidated through transmission electron microscopy (TEM), revealing a distinct cup-shaped morphology (Fig. 1A). Dynamic light scattering (DLS) measurements indicated sizes of approximately 148.6 nm for ME and 155.7 nm for KME, with zeta potentials around −10 mV (Fig. 1C). Fluorescent labeling of ME with DiI dye (red) and DSPE-PEG_{2000}-KDEL with FITC (green) demonstrated a high degree of colocalization (Fig. 1B), confirming the successful insertion of KDEL peptide into exosome membrane. Western blotting assay further verified the retention of key protein components from the ME, particularly TSG101, and CD63[35], within KME (Supporting Information Fig. S3), indicating the successful fabrication of KDEL-modified ME.

High entrapment efficiency and loading capacity of exosomes for CEL and siRNA were achieved. As shown in Supporting Information Table S1, CEL was efficiently loaded into ME and KME, with EE of approximately 80.2% and 86.8%, and LC of approximately 3.9% and 4.2%. The EE of siRNA loaded in ME and KME was 78.7% and 79.5%, respectively, with an LC of approximately 3.8%. The stability of exosomes in various physiological environments, including PBS, simulated gastric fluid (SGF), simulated intestinal fluid (SIF), and simulated colonic fluid (SCF), were then established, as evidenced by minimal changes in particle size and polydispersity index (PDI) of ME and KME (Supporting Information Fig. S4).

In vitro, the release behavior of CEL was explored in a PBS solution with pH 6.8. The cumulative CEL release in ME and KME was 23.4% and 19.0% at 24 h, and 53.1% and 43.3% at 144 h, respectively (Supporting Information Fig. S5). Moreover, ME and KME exhibited notable protection of siRNA against RNase degradation and the acid environment of the stomach in comparison to free siRNA, as confirmed by agarose gel electrophoresis (Supporting Information Figs. S6 and S7).

3.3. Cellular uptake, intracellular trafficking and distribution of KME

Next, we proceeded to investigate the potential of KDEL modification in effective ER-targeting of KME. After KDEL modification, the cellular uptake of KME was a little more than that of ME (Supporting Information Fig. S8), probably attributed to reduced lysosomal degradation. The CLSM images revealed that KME had superior colocalization with the ER and Golgi apparatus in comparison to ME (Fig. 1D). The colocalization coefficients of KME with the Golgi apparatus, ER, and lysosomes were determined to be 0.7, 0.8, and 0.2 (Fig. 1E), respectively. The noteworthy enhancement in ER retention behavior could be attributed to the KDEL decoration, recognized by KDEL receptors specifically distributed in the Golgi and ER[38]. Importantly, the lower colocalization ratio of KME with lysosomes (∼22.0%) indicated KME's effective avoidance of lysosomal degradation.

It has been reported that the COPI-coated vesicles allow the precise sorting of cargo between the Golgi apparatus and retrieval from the Golgi to the ER[39]. To further explore the ER-targeted trafficking mechanism of KME, GCA, a specific inhibitor inhibiting the assembly of COPI-coated vesicles[40], was utilized. After being pre-treated with GCA, the colocalization ratio of KME in the ER significantly decreased from 0.8 (without GCA) to 0.2 (with GCA), whereas the colocalization ratio in Golgi increased (Fig. 1E). This indicated KME's ER-targeting *via* the Golgi-ER pathway. Additionally, KME exhibited high fluorescence colocalization (∼75.0%) with COPI-coated vesicles (Fig. 1F), showing COPI-coated vesicles-mediated transportation of KME from Golgi to ER (Fig. 1G). These findings underscored that KDEL modification endowed KME with an effective ER-targeting capacity.

3.4. Amplification of the ICD effect by KME@CEL

To elucidate the impact of ER-targeted delivery of CEL on inducing the ICD effect, CEL-loaded ME and KME (denoted as ME@CEL and KME@CEL, respectively) were incubated with CT26 cells for 24 h. The cytotoxicity assessed through CCK-8 assay revealed increased cell death in both ME@CEL and KME@CEL groups compared to free CEL (Fig. 2A), with corresponding IC_{50} values of 1.9 and 1.7 μmol/L, respectively (Supporting Information Fig. S9). Flow cytometry analysis of apoptosis rates at a CEL concentration of 2.5 μM demonstrated

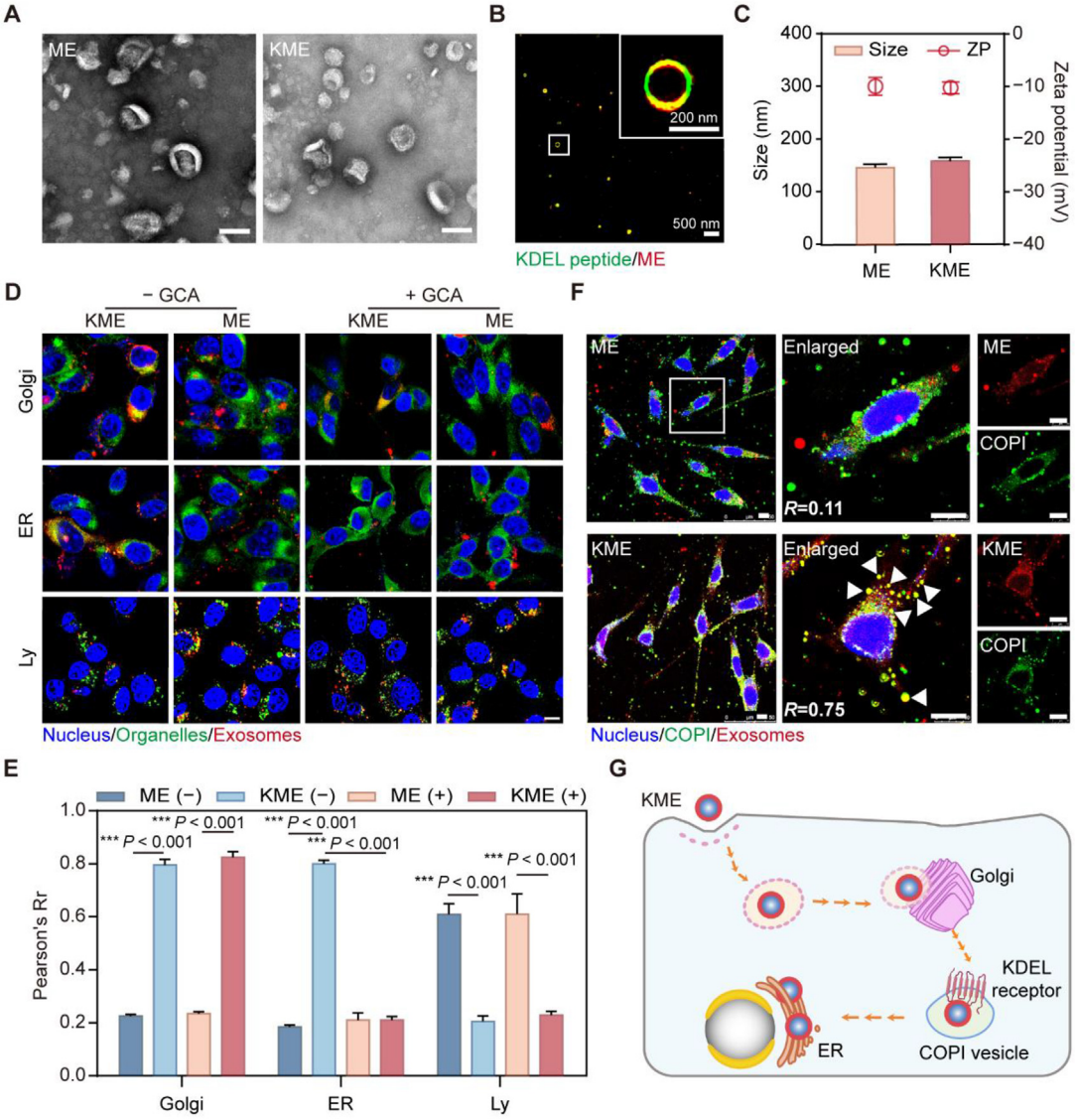

Figure 1 Preparation and characterization of ER-targeted exosomes. (A) TEM images of ME and KME. Scale bar = 100 nm. (B) Fluorescent colocalization analysis of KDEL peptide and ME. Red: ME; Green: DSPE-PEG_{2000}-KDEL. Scale bar = 500 and 200 nm (enlarged). (C) Particle size and zeta potential of ME and KME. (D) The CLSM images of ME or KME interacting with the Golgi apparatus, ER, and lysosomes (Ly) without GCA inhibition (left) and with GCA inhibition (right). Red: ME or KME; Green: organelles (Golgi apparatus, ER, and lysosomes); Blue: cell nucleus. Scale bar = 10 μm. (E) Pearson's correlation coefficient of ME, KME and the Golgi apparatus, ER, and lysosomes with or without GCA inhibition (n = 3). (F) CLSM colocalization images of ME and KME with COPI vesicles. Scale bar = 10 μm. (G) Schematic diagram of the KME intracellular trafficking pathways. Data are presented as mean ± SD; ***P < 0.001.

substantial increases in apoptotic potential for both ME@CEL (47.8%) and KME@CEL (64.6%), outperforming free CEL (7.5%) (Fig. 2B and C). Importantly, KME@CEL exhibited superior cytotoxicity and enhanced apoptosis compared to ME@CEL, potentially attributed to the ER-targeted delivery of CEL by KME, leading to intensified ER stress and autophagy.

To assess the enhanced ICD effect, the expression of proteins associated with ER stress and autophagy was investigated. CT26 cells treated with KME@CEL exhibited a significant increase in p-PERK expression, leading to a noteworthy enhancement in the p-PERK to total PERK protein ratio (Fig. 2D). Additionally, KME@CEL led to a decrease in caspase 3 expression, accompanied by a significant upregulation of c-caspase 9 and c-caspase 3 expression (Fig. 2D). KME@CEL increased the LC3-II/LC3-I ratio to 59.7%, significantly higher than that of the ME@CEL group and CEL group (Supporting Information Fig. S10). This indicated that KME@CEL could induce stronger autophagy.

Furthermore, the levels of three ICD effect markers, DAMPs including CRT, ATP, and HMGB1, were assessed. KME@CEL significantly increased CRT exposure and enhanced ATP and HMGB1 release (Fig. 2E−G). KME@CEL demonstrated substantial enhancements in ATP release (a 10.8-fold increase compared to PBS) and HMGB1 release (a 7.6-fold increase compared to PBS). These results indicated that ER-target exosomes markedly enhanced CEL's ability to induce immunogenic apoptosis of tumor cells.

DAMPs play a pivotal role in stimulating the transformation of immature DCs into mature phenotypes. The proportion of mature

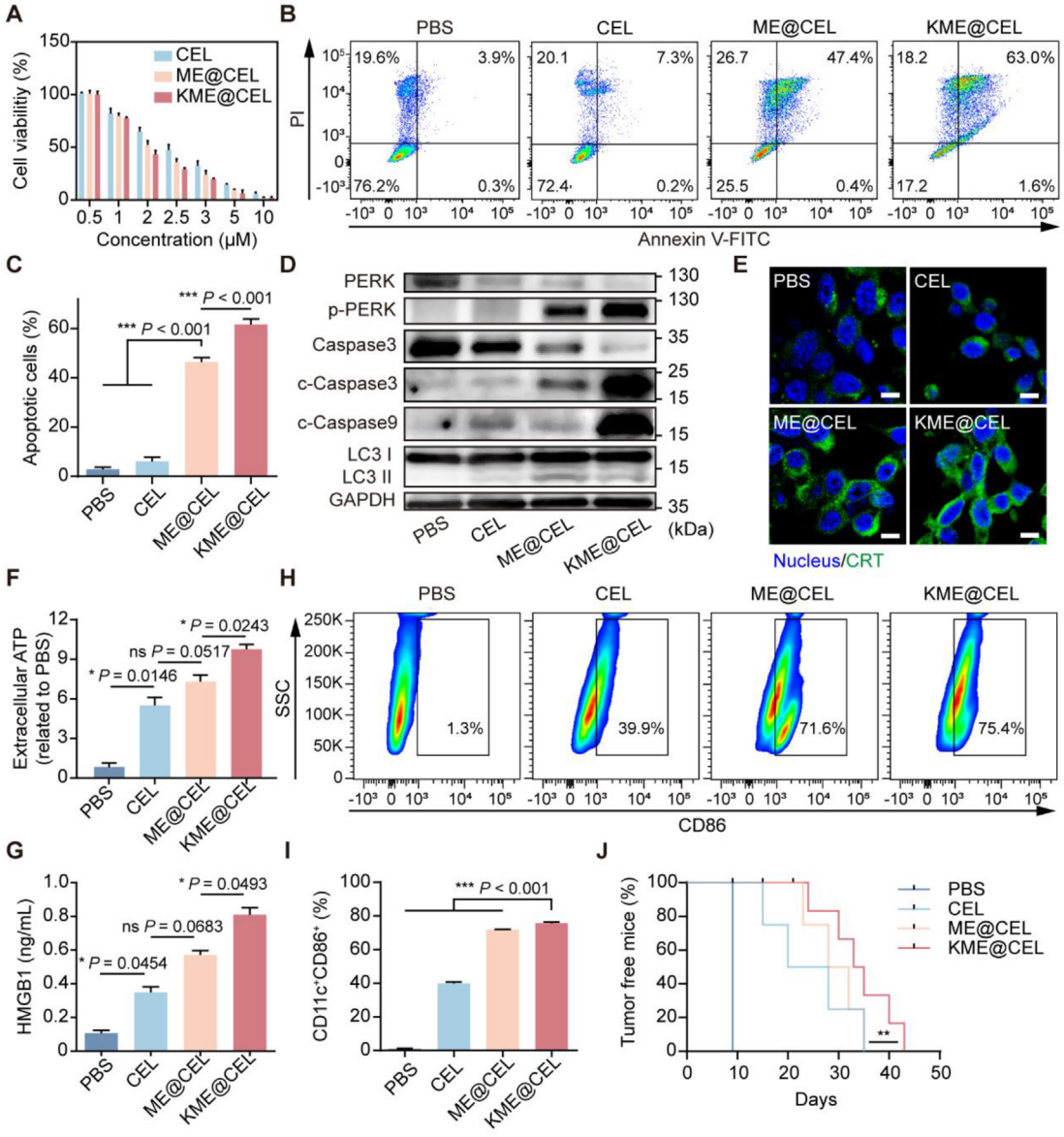

Figure 2 ER-targeted exosomes enhanced the ICD induction of CEL. (A) The cytotoxicity analysis of CEL, ME@CEL, and KME@CEL. (B, C) Flow cytometry evaluation and quantitative analysis of the apoptotic CT26 cells. CT26 cells were pre-treated with PBS, CEL, ME@CEL, and KME@CEL ($n = 3$). CEL dose, 2.5 μmol/L. (D) Western blot analysis of ER stress and autophagy-related proteins expression in CT26 cells pre-treated as indicated in (B, C) for 24 h. (E) CLSM images of the CRT exposure (green). Blue: cell nucleus. Scale bar = 10 μm. (F, G) Quantitative analysis of ATP secretion into the medium and the nuclear HMGB1 release ($n = 3$). BMDCs maturation determined by (H) flow cytometry and (I) quantification of the mature BMDCs ($CD11c^+CD86^+$). CT26 cells were pre-treated as indicated in (B, C) for 24 h; they were coincubated with BMDCs for another 48 h. (J) *In vivo* vaccination experiment using BALB/c mice ($n = 8$ mice per group). Data are presented as mean ± SD; ns. not significance; $^*P < 0.05$, $^{***}P < 0.001$.

DCs, as measured by flow cytometry, was significantly higher in the KME@CEL group (75.4%) compared to the free CEL (39.9%) and ME@CEL (71.6%) groups (Fig. 2H and I), confirming that the enhanced ICD induction by KME@CEL contributed to the promotion of DCs maturation.

To further validate the amplified ICD-inducing effect by ER-targeting, a gold-standard method of ICD detection, a vaccine experiment, was performed. Before the homogenous tumor challenge on Day 7, mice were inoculated with dying CT26 cells that had been treated with CEL, ME@CEL, or KME@CEL on Day 0 to induce T cell-mediated antitumor immunity against living cancer cells of the same kind *in vivo*[7]. The results demonstrated that vaccination with free CEL- or ME@CEL-treated cells resulted in a limited protective effect against tumor occurrence and growth (Fig. 2J). Of note, vaccination with KME@CEL-treated cells significantly retarded and suppressed subsequent tumor growth. In conclusion, ER-targeted delivery not only enhanced CEL-induced ICD in CRC cells but also more efficiently promoted the maturation of DCs and facilitated the development of robust anti-tumor immunity in mice.

3.5. Enhanced efficiency of gene silencing by KME@siPD-L1

Previous reports have revealed that delivering siRNA to ER could boost its gene silencing effects[41-42]. We then evaluated the gene silencing efficacy of siRNA-loaded KME. CLSM and flow cytometer results demonstrated that KME significantly enhanced the uptake of Cy3-labeled siRNA, surpassing the uptake in ME and free siRNA groups, and approaching the level of the positive control Lipo2000 group (Fig. 3A−C). Specifically, the KME group exhibited a 7.7- and 2.3-fold enhancement compared to free siRNA and ME, respectively. This enhancement could be attributed to KDEL modification, improving the targeting of siRNA to the ER and consequently reducing lysosomal degradation.

To delineate the intracellular trafficking pathway of siRNA after endocytosis, CLSM images of corresponding organelles were captured (Fig. 3D), and the fluorescence colocalization ratios were calculated based on Pearson's correlation coefficient. The colocalization coefficients of KME@Cy3 siRNA with Golgi apparatus, ER, and lysosome were 0.6, 0.7, and 0.2, respectively (Fig. 3E−G). Cy3 siRNA loaded in KME exhibited significant colocalization effects with ER and Golgi, but not lysosomes, whereas the fluorescence colocalization ratios of Cy3 siRNA from ME and Lipo2000 in lysosomes were approximately 69.2% and 53.1%. These findings indicated that KME was proficient in targeting siRNA to the ER, an optimal site for siRNA to exert its effects.

Effective downregulation of programmed death-ligand 1 (PD-L1) is crucial for cancer immunotherapy. We next explored whether the delivery of PD-L1 siRNA to the ER is more effective in promoting intracellular PD-L1 gene silencing. The distinct groups (PBS, free siPD-L1, ME@siPD-L1, KME@siPD-L1, and Lipo2000@siPD-L1) were incubated with CT26 cells, and Western blotting results demonstrated a significant reduction to 51.7% in the overall PD-L1 protein expression in the KME@siPD-L1 group (Fig. 3H). Specifically, KME@siPD-L1 exhibited a 1.9-, 1.8-, 1.4-, and 1.1-fold reduction compared to PBS, free siPD-L1, ME@siPD-L1, and Lipo2000@siPD-L1, respectively. By PE-CD274 antibody labeling, flow cytometry results further indicated that KME@siPD-L1 markedly suppressed the PD-L1 protein level of approximately 54.8% on the cell membrane (Fig. 3I and J). This outcome suggested that the reduction in intracellular PD-L1 protein abundance translates into a decrease in PD-L1 proteins on the cell membrane. KME@siPD-L1 demonstrated similar downregulation of PD-L1 protein with Lipo2000@siPD-L1 (52.6%). These comprehensive findings suggested that KME delivering PD-L1 siRNA to the ER significantly diminished PD-L1 protein expression on the cell membrane by downregulating overall PD-L1 protein expression. Therefore, the enhanced gene silencing effects of KME@siPD-L1 could be attributed to the improved uptake and the alteration in the intracellular trafficking pathway of siRNA.

3.6. In vitro immunological assessment of CEL/siRNA-coloaded formulation

Having established the enhanced ICD effect induced by CEL and the improved gene silencing efficiency of PD-L1 siRNA, we proceeded to evaluate the *in vitro* immunological effects of CEL and PD-L1 siRNA-coloaded KME. Six different formulations (G1: PBS; G2: Free CEL+siPD-L1; G3: KME@CEL; G4: KME@siPD-L1; G5: ME@CEL+siPD-L1; G6: KME@CEL+siPD-L1) were prepared and incubated with CT26 cells. The impact of the CEL/siRNA-coloaded formulation on improving PD-L1 gene silencing was assessed by quantifying PD-L1 mRNA levels through RT-qPCR. The results indicated that the KME@CEL+siPD-L1 group, attributed to the ER-targeting advantage, showed 74.5% downregulation of PD-L1 mRNA, which exhibited approximately a 2.1-fold higher downregulation compared to ME@CEL+siPD-L1 (Fig. 4A). This reduction in PD-L1 mRNA levels corresponded to a decrease in PD-L1 protein expression. Immunofluorescence staining and flow cytometry were employed to examine total PD-L1 protein levels and PD-L1 protein on the cell membrane, respectively. The KME@CEL+siPD-L1 group demonstrated a 4.1-, 2.3-, 2.5-, 2.1-, and 1.3-fold reduction in the levels of PD-L1 protein on the cell membrane compared to PBS, CEL+siPD-L1, KME@CEL, KME@siPD-L1, and ME@CEL+siPD-L1, respectively (Fig. 4B and C). Consistently, the KME@CEL+siPD-L1 group demonstrated an obvious reduction in total PD-L1 protein expression compared to the single drug-loaded group and non-targeting group (Fig. 4D and E). These findings demonstrated that KME@CEL+siPD-L1 displayed significantly higher gene silencing effects than KME@CEL and KME@siPD-L1, suggesting a potential synergistic effect between CEL and PD-L1 siRNA in PD-L1 suppression.

In addition, we also examined the *in vitro* biocompatibility of KME@CEL+siPD-L1 on normal cells. NCM640 cells, a human normal intestinal epithelial cell line, were chosen as the cell model. The CCK-8 analysis results indicated that the IC_{50} values of KME@CEL and KME@CEL+siPD-L1 in NCM460 cells exceeded our therapeutic doses, demonstrating good biocompatibility with normal cells (Supporting Information Fig. S11). Furthermore, the flow cytometry results demonstrated that the uptake efficiency of CT26 cells for KME was notably higher than that of NCM460 cells at carrier concentrations of 40 μg/mL and 100 μg/mL, possibly due to the heightened demand for nutrients by tumor cells (Supporting Information Fig. S12).

CEL-induced ICD and the release of DAMPS and promoted tumor antigen presentation by DCs. Simultaneously, the PD-1/PD-L1 axis serves as a negative modulatory signaling pathway that triggers immunosuppressive effects, including T cell anergy[9]; thus, blocking PD-1 or PD-L1 using antibodies[43-44] or downregulating PD-L1 expression[45-46] was shown to promote the functions and proliferation of T cells. To investigate the effects of different agent groups on T cell activation, spleen lymphocytes (SPLCs) were separated from BALB/c mice and utilized to construct a CT26-BMDCs-T cell coculture model (Fig. 4F). T cells consist of helper T cells, cytotoxic T cells, regulatory T cells, and memory T cells, among which cytotoxic T cells play a crucial role in recognizing and eliminating infected or abnormal cells[10,47]. The proliferation and activation of T cells were examined by measuring the number of $CD8^+$ T cells *via* flow cytometry. In the KME@CEL+siPD-L1 group, the proportion of cytotoxic T cells was 10.5%, significantly surpassing the rates of 5.2% in the PBS group, 6.2% in the Free CEL+siPD-L1 group, 6.5% in the KME@CEL group, 7.4% in the KME@siPD-L1 group, and 8.4% in the ME@CEL+siPD-L1 group (Fig. 4G and H). Overall, tumor cells treated with ER-targeting KME@CEL+siPD-L1 efficiently induced T cell activation, especially $CD8^+$ T cells. These findings highlight the potential of the KME@CEL+siPD-L1 to promote a robust immunological response against cancer cells.

3.7. Colon targeting and tumor accumulation capabilities

The oral route is preferred for CRC patients, and milk-derived exosomes have emerged as promising vehicles for oral drug

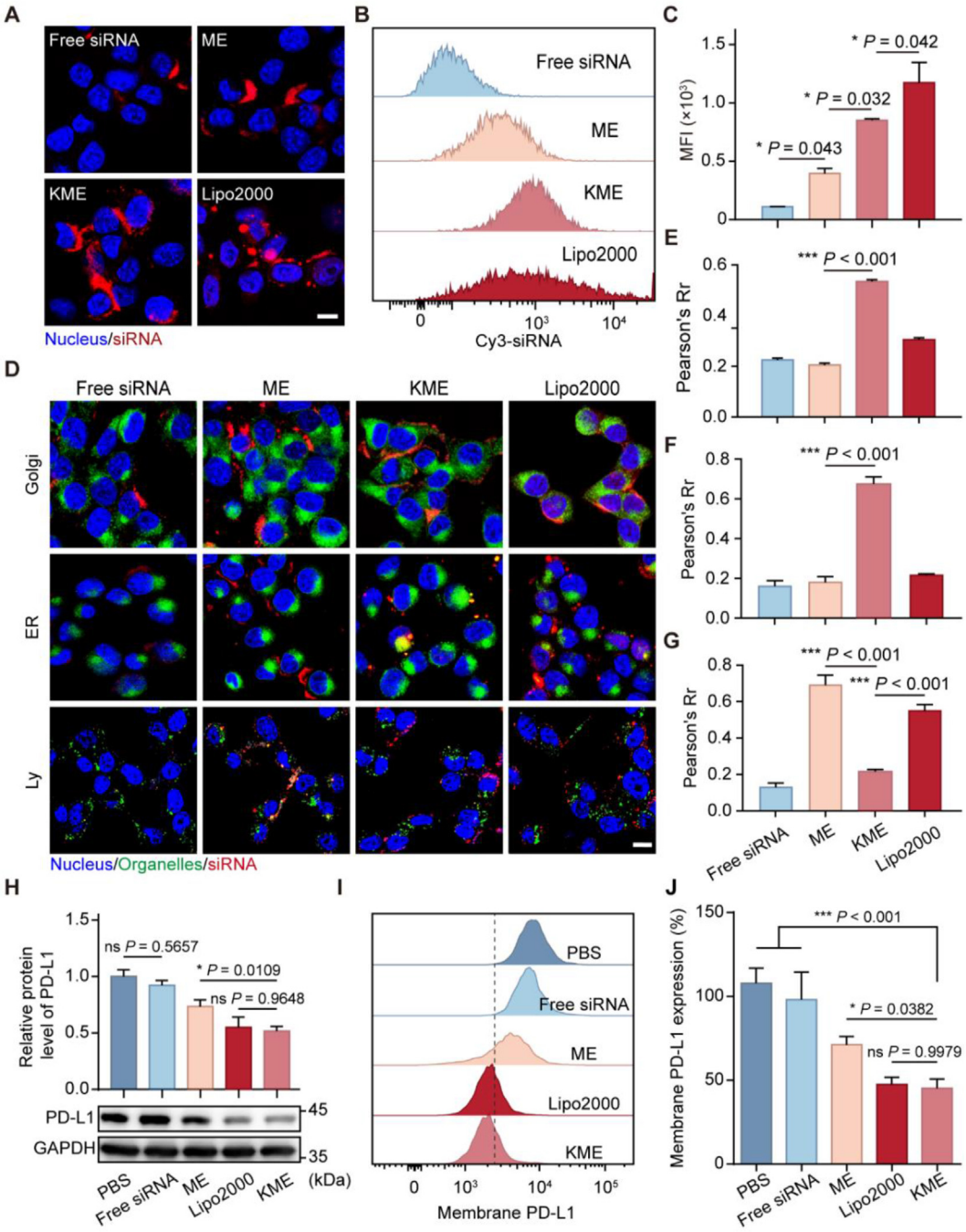

Figure 3 ER-targeting enhanced gene silencing efficiency of PD-L1 siRNA *in vitro*. (A) CLSM images of CT26 cells after 2-h incubation with free siRNA, ME@siRNA, KME@siRNA, and Lipo2000@siRNA. The siRNA was labeled with Cy3 (red), and the cell nuclei were stained with DAPI (blue). Scale bar = 10 μm. (B, C) The quantitative analysis of Cy3 siRNA uptake efficiency by flow cytometry ($n = 3$). (D, G) CLSM images (D) and Pearson's correlation coefficient of siRNA interacting with the Golgi apparatus (E), ER (F), and lysosomes (G) ($n = 3$). Red: Cy3-labeled siRNA; Green: organelles (Golgi apparatus, ER, and lysosomes); Blue: cell nucleus. Scale bar = 25 μm. (H) Western blotting analysis and quantitative analysis the expression of overall PD-L1 protein in CT26 cells pre-treated with PBS, free siPD-L1, ME@siPD-L1, KME@siPD-L1, and Lipo2000@siPD-L1 for 48 h. (I, J) Flow cytometry evaluation and quantitative analysis of the expression of membrane PD-L1 protein. Data are presented as mean ± SD; ns, not significance; $*P < 0.05$, $***P < 0.001$.

delivery[34,48]. Meanwhile, oral administration of siRNAs represents a breakthrough approach in the field of nucleic acid therapy, offering several advantages over traditional delivery methods. By bypassing invasive procedures such as intravenous injections, oral delivery provides a non-invasive and patient-friendly approach[49]. Additionally, oral administration of siRNA enables targeted delivery in the gastrointestinal tract, leading to more precise and effective treatment of localized diseases such as colorectal cancer[35]. Direct targeting of tumor cells in the colon through oral administration is anticipated to

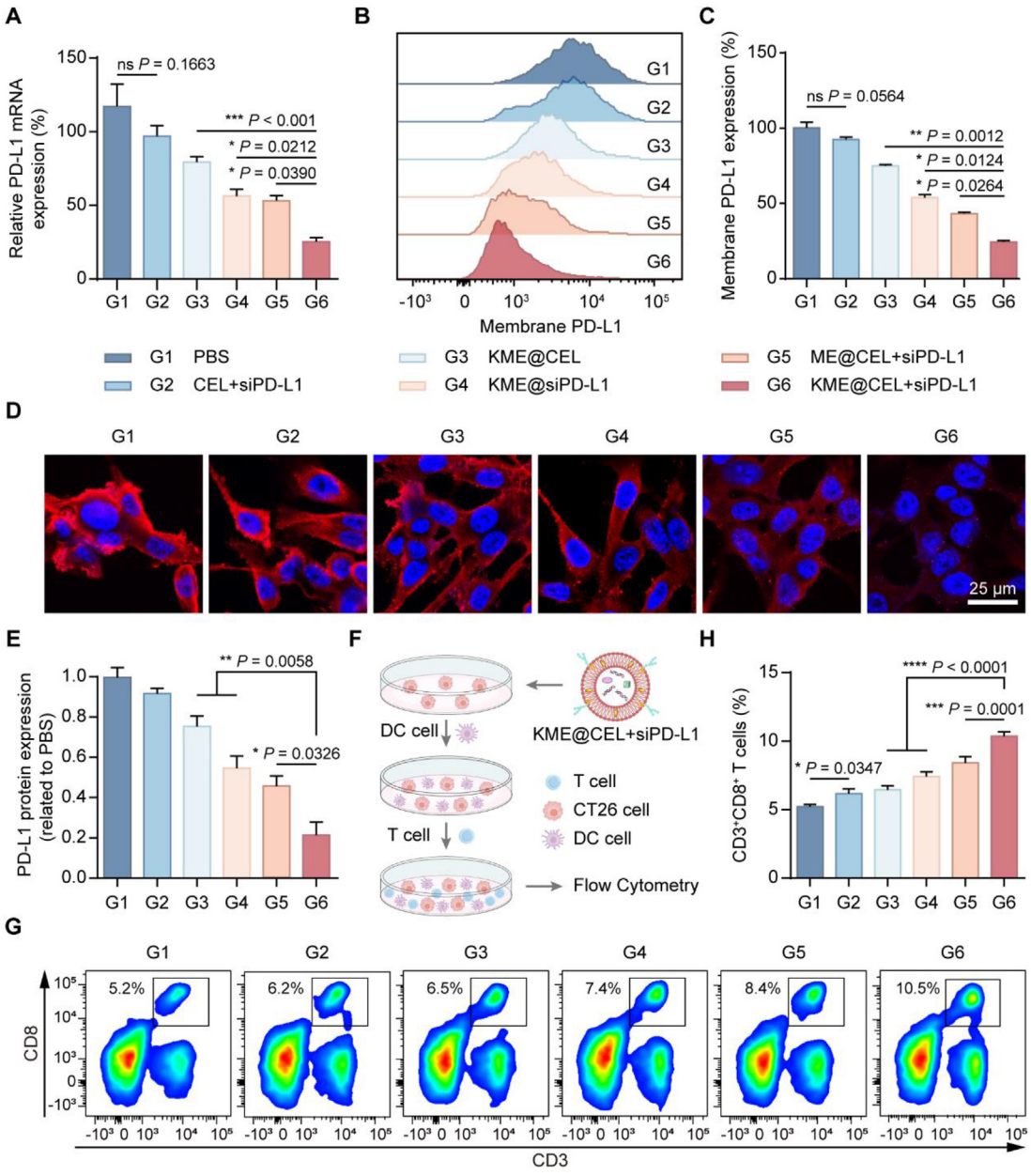

Figure 4 The immune responses activated by CEL/siRNA-coloaded formulation *in vitro*. (A) RT-qPCR examination of PD-L1 mRNA expression levels ($n = 3$). G1: PBS; G2: CEL+siPD-L1; G3: KME@CEL; G4: KME@siPD-L1; G5: ME@ CEL+siPD-L1; G6: KME@CEL+siPD-L1. (B, C) Flow cytometry and quantitative analysis of the expression of PD-L1 protein on the cell membrane ($n = 3$). (D, E) Immunofluorescence staining and quantitative analysis of the expression of PD-L1 protein throughout the cells ($n = 3$). Scale bar = 25 μm. (F) Schematic diagram of the CT26-BMDCs-T cell coculture model. (G, H) Flow cytometry examination and quantitative analysis of cytotoxic T cells during the coculture experiment ($n = 3$). Data are mean ± SD; ns, not significance; $^{*}P < 0.05$, $^{**}P < 0.01$, $^{***}P < 0.001$, $^{****}P < 0.0001$.

enhance therapeutic efficacy while minimizing systemic toxicity[50].

Despite the advantages of oral formulations, they encounter physiological barriers such as colonic mucus penetration and epithelial cell transport[51-52]. To address these challenges, we explored the potential of KME as an oral drug delivery system, specifically investigating their ability to overcome colonic mucus and epithelial cell transport barriers. By fluorescently labeling the mucus with Alexa Fluor 488-conjugated WGA, we uncovered that DiI-labeled ME and KME efficiently penetrated the colonic mucus, facilitating absorption by colonic epithelial cells (Fig. 5A). To further examine the transepithelial pathway and efficiency of exosomes, Caco-2 cell monolayers in Transwell models were established referenced our previous study[53]. The results showed that both ME and KME exhibited superior transepithelial efficiency (approximately 23.4% and 29.0%) than PEGylated liposomes (8.8%) (Fig. 5B) after incubation for 8 h.

FcRn is a receptor expressed in the intestines of both humans and mice[54-55]. ME and KME were found to largely colocalize with FcRn receptors in Caco-2 cell monolayers (Fig. 5C), confirming the FcRn-mediated transepithelial trafficking mechanism[56]. Utilizing double fluorophores-labeled ME@FAM-siRNA and

KME@FAM-siRNA, we observed an intense FRET spectrum in the basolateral medium, verifying the transepithelial transport of intact exosomes (Fig. 5D). The anti-tumor effect was evaluated post-transportation across the mucus and cell monolayer. In the basolateral chamber, CT26 cells were inoculated, and images revealed that both KME@CEL+siPD-L1 and ME@CEL+siPD-L1 effectively induced cancer cell apoptosis after crossing the intestinal epithelial cells (Fig. 5E). These results collectively highlighted the potential of milk-derived exosomes to overcome colonic physiological barriers, making them promising oral drug delivery systems for CRC therapy.

Using the CT26-Luc-derived orthotopic CRC mouse model, we then assessed the tissue distribution and tumor accumulation of milk-derived exosomes *in vivo*. Twelve hours post oral administration of DiR-labeled exosomes, mice, and excised major tissues and intestines were imaged using the IVIS Kinetics Optical System. Simultaneously, orthotopic colorectal tumors of mice were also imaged by luciferin (i.p.). The results indicated that both ME and KME achieved significantly high retention in tumors (Fig. 5F, Supporting Information Figs. S13 and S14). This could be attributed to the efficient mucus permeation and *trans*-epithelial cell uptake by milk exosomes. In contrast, the free DiR dye group exhibited minimal accumulation in CRC (Fig. S8). Additionally, the ER-targeted capacity of KME *in vivo* was evaluated through immunofluorescence staining. Consistent with the *in vitro* colocalization results, KME exhibited significant colocalization signals with ER and Golgi (Fig. 5G). The colocalization coefficients of KME with Golgi apparatus, ER, and lysosome were 0.8, 0.7, and

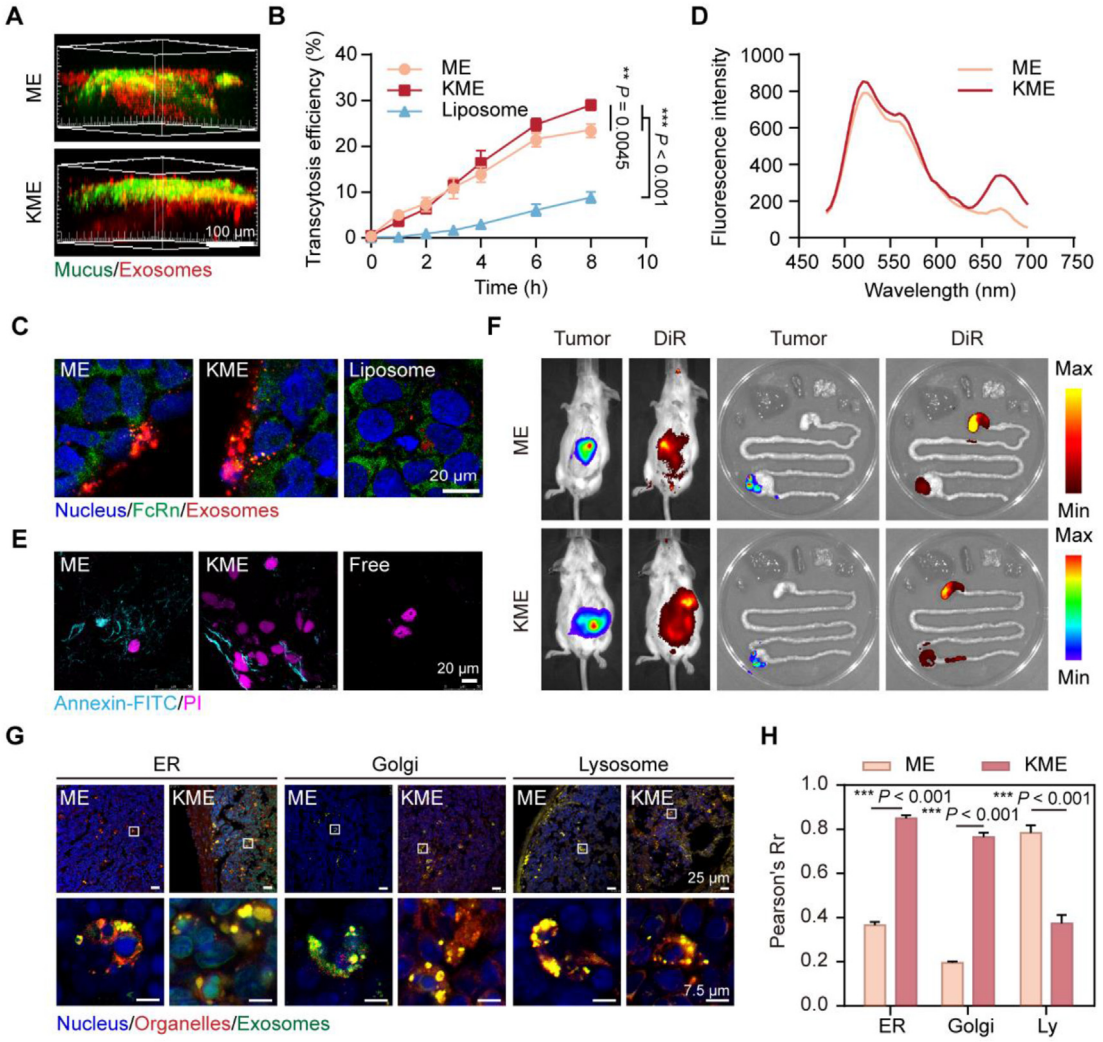

Figure 5 Colonic mucus and epithelium barriers overcoming and tumor accumulation of milk-derived exosomes. (A) 3D images of colonic mucus penetration of KME and ME. Red: ME or KME; Green: mucus stained with Alexa Fluor 488-wheat germ agglutinin. Scale bar = 100 μm. (B) The transepithelial efficiency of KME, ME, and liposome across the epithelial cells (n = 3). (C) Immunofluorescence staining analysis of FcRn-mediated transcytosis pathway of KME and ME. Scale bar = 20 μm. (D) Emission spectra of siRNA-loaded ME and KME with excitation at 450 nm. (E) Tumor cell apoptosis after transcytosis for KME@CEL+siPD-L1, ME@CEL+siPD-L1, and Free CEL+siPD-L1. Scale bar = 20 μm. (F) *In vivo* imaging of the colon-targeting and tumor accumulation of KME and ME at 12 h following oral administration. (G, H) Colocalization analysis of ME and KME with the Golgi apparatus, ER, and lysosomes (Ly) within tumor tissues. Red: ME or KME; Red: organelles (Golgi apparatus, ER, and lysosomes); Blue: cell nucleus (n = 3). Scale bar = 25 μm (top) and 7.5 μm (bottom). Data are mean ± SD; $^{**}P < 0.01$, $^{***}P < 0.001$.

0.3, respectively (Fig. 5H). These results emphasized that the KDEL modification on KME maintained its ER-targeting function *in vivo*, which could facilitate the effective delivery of drugs to the ER in tumor tissues and augment anti-tumor treatment.

3.8. *In vivo anti-tumor efficacy evaluation in orthotopic CRC model*

The therapeutic effects of KME@CEL+siPD-L1 were assessed in BALB/c mice bearing CT-26-Luc colonic orthotopic xenografts. Ten days after tumor inoculation (designated as Day 0), mice were randomized into five groups: Saline, KME@CEL, KME@siPD-L1, ME@CEL+siPD-L1, KME@CEL+siPD-L1 (n = 5 mice per group). Treatments were administrated once every two days (Fig. 6A). As CT26-Luc cells stably express the firefly luciferase gene, allowing monitoring of tumor growth *in situ*[57], bioluminescence imaging with the IVIS Kinetics Optical System was employed. Before living imaging, we confirmed the linear correlation between the number of CT26-Luc cells and bioluminescence intensity (Fig. 6B). The bioluminescence imaging results revealed varying degrees of tumor suppression after the various treatments, with the KME@CEL+siPD-L1 group consistently maintaining tumor size at a low level (Fig. 6C). Importantly, the KME@CEL+siPD-L1 group exhibited a significantly stronger tumor-suppressive effect than the ME@CEL+siPD-L1 group, indicating that codelivery of CEL and PD-L1 siRNA to the ER effectively triggered endogenous anti-tumor responses, thus successfully inhibiting tumor growth (Fig. 6D). The hematoxylin−eosin (H&E) and the deoxynucleotidyl transferase-mediated dUTP-biotin nick end labeling (TUNEL) staining results further demonstrated that the KME@CEL+siPD-L1 group effectively promoted cancer cell apoptosis (Fig. 6F and G). Notably, the KME@CEL+siPD-L1 group

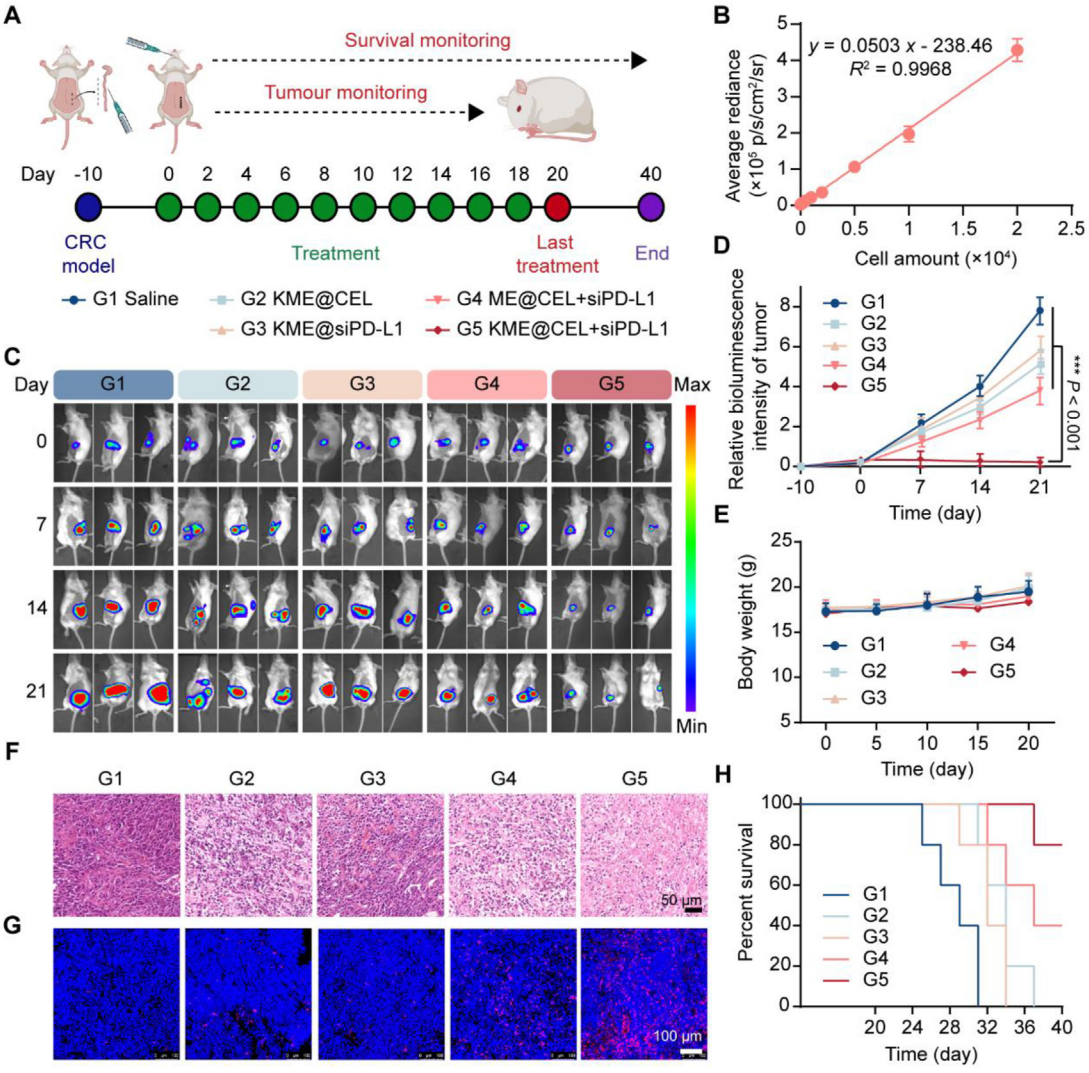

Figure 6 *In vivo* tumor growth inhibition studies in an orthotopic CRC mice model. (A) Therapeutic schedule for *in vivo* combination colorectal cancer. G1: Saline; G2: KME@CEL; G3: KME@siPD-L1; G4: ME@CEL+siPD-L1; G5: KME@CEL+siPD-L1 (n = 5). (B) Linear correlation between the number of CT26-Luc cells and bioluminescence intensity. (C) *In vivo* imaging of tumor growth in G1-G5 groups after oral administration at different times. (D) Quantitative analysis of bioluminescence intensity of tumor in G1-G5 groups (n = 5). (E) Body weights of mice in different groups (n = 5). (F) H&E staining of tumor tissues. Scale bar = 50 μm. (G) TUNEL staining of tumor tissues. Scale bar = 100 μm. (H) Survival curve of BALB/c mice (n = 5). Data are mean ± SD; ***P < 0.001.

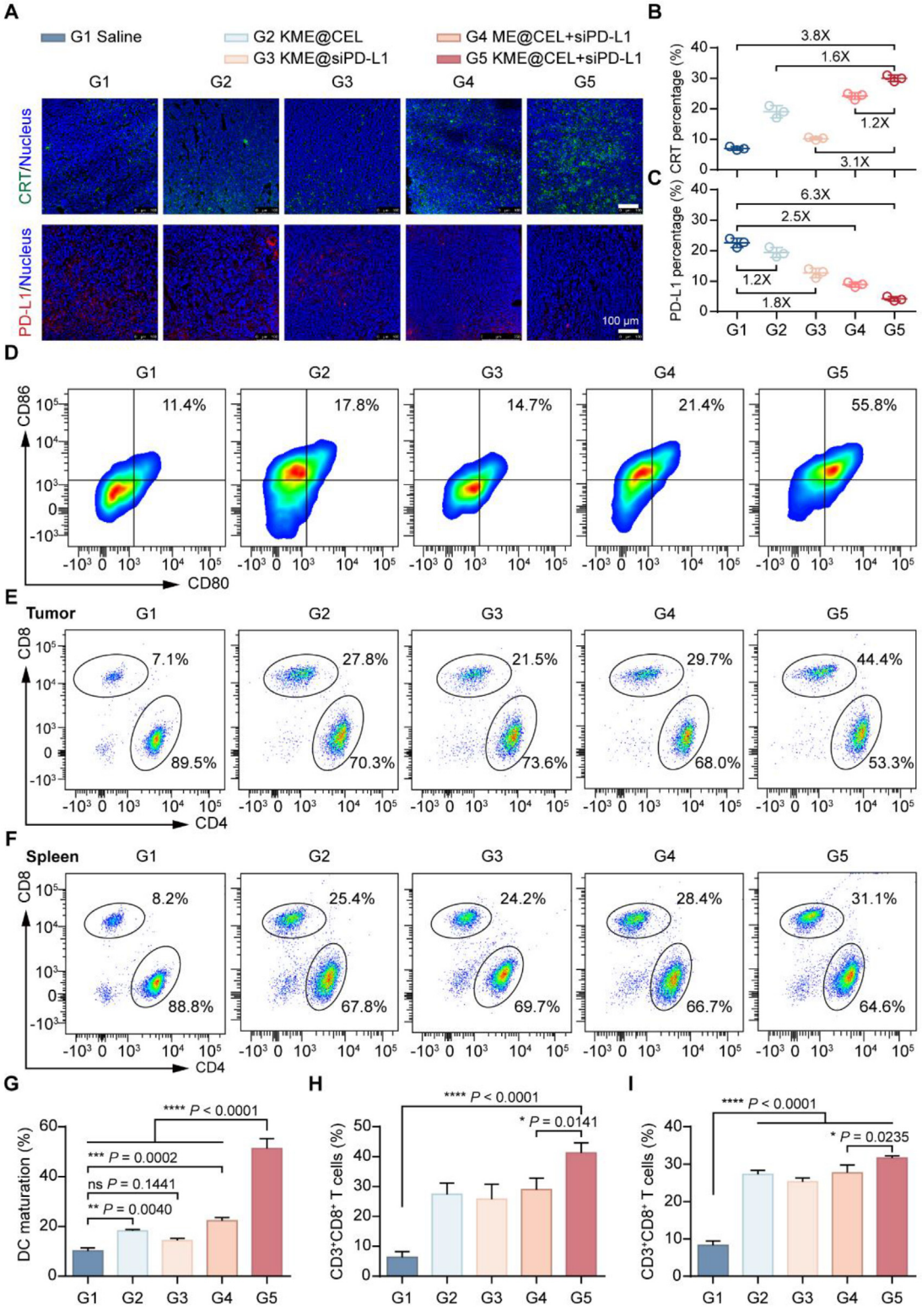

Figure 7 *In vivo* anti-tumor immune responses of the CT26 tumor-bearing BALB/c mice. CRT exposure and PD-L1 expression in the tumors by (A) immunostaining (green: CRT; red: PD-L1; blue: DAPI; scale bar = 100 μm) and the quantification of (B) CRT exposure and (C) PD-L1 expression by ImageJ. G1: saline; G2: KME@CEL; G3: KME@siPD-L1; G4: ME@CEL+siPD-L1; G5: KME@CEL+siPD-L1. (D, G) Flow cytometry analysis of the mature DCs in mesenteric lymph nodes of BALB/c mice: (D) the contour diagrams and (G) quantification; $n = 3$ mice. (E, H) Flow cytometry analysis of cytotoxic T cells in the tumors of BALB/c mice: (E) the contour diagrams and (H) quantification; $n = 3$ mice. (F, I) Flow cytometry analysis of cytotoxic T cells in the spleen of BALB/c mice: (F) the contour diagrams and (I) quantification; $n = 3$ mice. Data are mean ± SD; ns, not significance; $^{*}P < 0.05$, $^{**}P < 0.01$, $^{***}P < 0.001$, $^{****}P < 0.0001$.

displayed a prolonged overall survival time, maintaining an 80.0% survival rate at the end of the experiment (Fig. 6H). This suggested that the endogenous antitumor response induced by KME@CEL+siPD-L1 could sustainably inhibit tumor growth, making it an effective therapeutic strategy for CRC therapy.

Moreover, the CEL/PD-L1 siRNA-coloaded exosomes were well-tolerated at the administrated doses, as evidenced by normal body weight gains (Fig. 6E), normal histology of major organs examined (Supporting Information Fig. S15), and minimal changes in the serum levels of ALT, AST, BUN and CRE (Supporting Information Fig. S16), suggesting the biosafety of CEL/PD-L1 siRNA-coloaded KME *in vivo*.

3.9. *In vivo assessment of immune responses*

The effectiveness of KME@CEL+siPD-L1 in inhibiting the growth of orthotopic CRC in BALB/c mice prompted the exploration of the *in vivo* immune responses. The immunofluorescence staining of CRT protein and PD-L1 protein in tumor tissue sections unveiled an augmented exposure of CRT protein in the KME@CEL+siPD-L1 group, exhibiting a 3.8-, 1.6-, 3.1-, and 1.2-fold higher fluorescence compared to saline, KME@CEL, KME@ siPD-L1 and ME@CEL+siPD-L1, respectively (Fig. 7A and B). Simultaneously, the expression of PD-L1 protein in the tumor tissues of the KME@CEL+siPD-L1 group was significantly downregulated, reaching only 18.6% of the saline group (Fig. 7A and C).

CRT is indicative of the extent of ICD in tumor tissues. The release of immunogenic factors post-ICD in tumors can stimulate the maturation of DCs. Flow cytometry analysis of $CD80^+$ and $CD86^+$, biomarkers of mDCs[58], in DCs from mesenteric lymph nodes revealed a remarkable increase in KME@CEL+siPD-L1, with 55.8% $CD80^+CD86^+$ mDCs, significantly surpassing those of other groups (Fig. 7D and G).

The mDCs play a pivotal role in presenting antigens to T cells and promoting the recruitment of T cells into tumors. Concurrently, the decreased expression of PD-L1 protein also fosters T cell activation. Notably, KME@CEL+siPD-L1 treatment recruited 44.4% $CD8^+$ T cells into tumors, significantly higher than the ME@CEL+siPD-L1 group (29.7%) (Fig. 7E and H). Furthermore, analysis of lymphocytes from spleens demonstrated a remarkable increase in the proportion of cytotoxic T cells in the KME@CEL+siPD-L1 group (31.1%) compared to the other groups (Fig. 7F and I). The low population of $CD8^+$ T cells in the tumor and spleen with KME@siPD-L1 treatment was attributed to inadequate tumor infiltration of T cells. These findings underscored the significant enhancement of endogenous antitumor responses by KME@CEL+siPD-L1, promoting ICD and reducing PD-L1 protein expression in tumor-bearing mice. As expected, the mice in the KME@CEL+siPD-L1 group had significantly higher levels of circulating cytokines, including TNF-α, and IL-6 than mice in other groups (Supporting Information Fig. S17). Therefore, the effectiveness of delivering CEL and PD-L1 siRNA to the endoplasmic reticulum emerges as a potent strategy for tumor chemoimmunotherapy.

4. Conclusions

In summary, our investigation into delivering ICD inducers and PD-L1 siRNA to ER has unveiled a potent and synergistic chemoimmunotherapeutic approach for CRC. The pivotal aspect of our strategy involved achieving ER-targeted delivery through the integration of KDEL peptide-modified milk-derived exosomes (KME). This tailored delivery system facilitated the accumulation of CEL, an ICD inducer, within the ER, thereby inducing robust ER stress, autophagy, and ICD. This cascade of events further promoted the maturation of DCs and significantly enhanced the infiltration of $CD8^+$ T cells into the tumor microenvironment. Concurrently, PD-L1 siRNA, guided to the ER, effectively silenced both intracellular and membrane PD-L1 protein expression, thereby activating T-cell responses. Collectively, an improved tumor suppression effect was achieved in orthotopic CRC BALB/c mice models, accompanied by the activation of an endogenous anti-tumor response. In light of the compelling efficacy observed in this study, our ER-targeted approach holds considerable promise for further efficacy testing in other highly appealing tumor types. This combination of ICD inducers and nucleic acid-based immunotherapy, orchestrated through ER-targeted delivery, presents a novel and promising avenue for advancing cancer treatment strategies.

Acknowledgments

The authors would sincerely appreciate the financial support from the National Science Fund of Distinguished Young Scholars (No. 82025032, China), the National Natural Science Foundation of China (No. 82073773, China), the Key Research Program of Chinese Academy of Sciences (No. ZDBS-ZRKJZ-TLC005, China), the "Open Competition to Select the Best Candidates" Key Technology Program for Nucleic Acid Drugs of NCTIB (No. NCTIB2022HS01006, China), Young Elite Scientists Sponsorship Program by CAST (No. 2022QNRC001, China), Shanghai Action Plan for Science, Technology, and Innovation (No. 23HC1401200, China), Shanghai Post-doctoral Excellence Program (No. 2022693, China) and Shanghai Institute of Materia Medica, Chinese Academy of Sciences (No. SIMM0220232001, China).

We thank the staff members of the Integrated Laser Microscopy System, the Electron Microscopy System, and the Large-scale Protein Preparation System at the National Facility for Protein Science in Shanghai (NFPS), Shanghai Advanced Research Institute, Chinese Academy of Sciences, China for sample preparation data collection and analysis. We are also very grateful to Guangyi Li, Yang Yu, Lihui Xin, Yanke Wang, and Fengming Liu for TEM data collection and Cell imaging data collection, respectively.

Author contributions

Miaorong Yu supervised the project. Miaorong Yu, Yong Gan, and Rui Wang designed the research and revised the manuscript. Jie Wang and Zilong Zhang carried out the experiments and performed data analysis. Yan Zhuo, Zhuan Zhang, Rongrong Chen, Li Liang, Xiang Li, and Jiaxin Li participated in part of the experiments. Chang Liu, Zhiwen Zou, Yong Gan, and Miaorong Yu provided resources. Jie Wang, Zilong Zhang, Xiaohe Jiang, and Miaorong Yu wrote the manuscript. All authors have read and approved the final manuscript.

Conflicts of interest

The authors have no conflicts of interest to declare.

Appendix A. Supporting information

Supporting information to this article can be found online at https://doi.org/10.1016/j.apsb.2024.04.010.

References

1. Mu WW, Chu QH, Liu YJ, Zhang N. A review on nano-based drug delivery system for cancer chemoimmunotherapy. *Nanomicro Lett* 2020;**12**:142.
2. Zhang YY, Zhang ZM. The history, and advances in cancer immunotherapy: understanding the characteristics of tumor-infiltrating immune cells and their therapeutic implications. *Cell Mol Immunol* 2020;**17**:807−21.
3. Salas-Benito D, Perez-Gracia JL, Ponz-Sarvise M, Rodriguez-Ruiz ME, Martinez-Forero I, Castanon E, et al. Paradigms on immunotherapy combinations with chemotherapy. *Cancer Discov* 2021;**11**:1353−67.
4. Sordo-Bahamonde C, Lorenzo-Herrero S, Gonzalez-Rodriguez AP, Martinez-Perez A, Rodrigo JP, Garcia-Pedrero JM, et al. Chemo-Immunotherapy: a new trend in cancer treatment. *Cancers (Basel)* 2023;**15**:2912.
5. Mu XP, Zhang M, Wei AH, Yin F, Wang Y, Hu KB, et al. Doxorubicin and PD-L1 siRNA co-delivery with stem cell membrane-coated polydopamine nanoparticles for the targeted chemoimmunotherapy of PCa bone metastases. *Nanoscale* 2021;**13**:8998−9008.
6. Tran TH, Phuong Tran TT. Targeting the PD-1/PD-L1 axis for cancer treatment: a review on nanotechnology. *R Soc Open Sci* 2022;**9**:211991.
7. Garcia-Gonzalez J, Ruiz-Banobre J, Afonso-Afonso FJ, Amenedo-Gancedo M, Areses-Manrique MDC, Campos-Balea B, et al. PD-(L)1 inhibitors in combination with chemotherapy as first-line treatment for non-small-cell lung cancer: a pairwise meta-analysis. *J Clin Med* 2020;**9**:2093.
8. Li CY, Han XP. Melanoma cancer immunotherapy using PD-L1 siRNA and imatinib promotes cancer-immunity cycle. *Pharm Res (N Y)* 2020;**37**:109.
9. Doroshow DB, Bhalla S, Beasley MB, Sholl LM, Kerr KM, Gnjatic S, et al. PD-L1 as a biomarker of response to immune-checkpoint inhibitors. *Nat Rev Clin Oncol* 2021;**18**:345−62.
10. Waldman AD, Fritz JM, Lenardo MJ. A guide to cancer immunotherapy: from T cell basic science to clinical practice. *Nat Rev Immunol* 2020;**20**:651−68.
11. Ya Z, Guo SF, Li Y, Zhu MT, Zhang L, Zong YJ, et al. Focused acoustic vortex-mediated sonochemotherapy for the amplification of immunogenic cell death combined with checkpoint blockade to potentiate cancer immunotherapy. *Biomaterials* 2023;**301**:122278.
12. Deng HZ, Zhou ZJ, Yang WJ, Lin LS, Wang S, Niu G, et al. Endoplasmic reticulum targeting to amplify immunogenic cell death for cancer immunotherapy. *Nano Lett* 2020;**20**:1928−33.
13. Liu Y, Jia HR, Han XF, Wu FG. Endoplasmic reticulum-targeting nanomedicines for cancer therapy. *Smart Mater Med* 2021;**2**:334−49.
14. Qiao L, Shao XX, Gao SJ, Ming Z, Fu XJ, Wei QC. Research on endoplasmic reticulum-targeting fluorescent probes and endoplasmic reticulum stress-mediated nano anticancer strategies: a review. *Colloids Surf B Biointerfaces* 2021;**208**:112046.
15. Li W, Yang J, Luo LH, Jiang MS, Qin B, Yin H, et al. Targeting photodynamic and photothermal therapy to the endoplasmic reticulum enhances immunogenic cancer cell death. *Nat Commun* 2019;**10**:3349.
16. Chen X, Cubillos-Ruiz JR. Endoplasmic reticulum stress signals in the tumour and its microenvironment. *Nat Rev Cancer* 2021;**21**:71−88.
17. Chen XY, Shi CR, He MH, Xiong SQ, Xia XB. Endoplasmic reticulum stress: molecular mechanism and therapeutic targets. *Signal Transduct Targeted Ther* 2023;**8**:352.
18. Aria H, Rezaei M. Immunogenic cell death inducer peptides: a new approach for cancer therapy, current status and future perspectives. *Biomed Pharmacother* 2023;**161**:114503.
19. Zhang JL, Sun XY, Zhao XF, Yang CR, Shi MH, Zhang BZ, et al. Combining immune checkpoint blockade with ATP-based immunogenic cell death amplifier for cancer chemo-immunotherapy. *Acta Pharm Sin B* 2022;**12**:3694−709.
20. Stalder L, Heusermann W, Sokol L, Trojer D, Wirz J, Hean J, et al. The rough endoplasmatic reticulum is a central nucleation site of siRNA-mediated RNA silencing. *EMBO J* 2013;**32**:1115−27.
21. Vincenz-Donnelly L, Hipp MS. The endoplasmic reticulum: a hub of protein quality control in health and disease. *Free Radic Biol Med* 2017;**108**:383−93.
22. Vaswani K, Mitchell MD, Holland OJ, Qin Koh Y, Hill RJ, Harb T, et al. A method for the isolation of exosomes from human and bovine milk. *J Nutr Metab* 2019;**2019**:5764740.
23. Crescitelli R, Lasser C, Lotvall J. Isolation and characterization of extracellular vesicle subpopulations from tissues. *Nat Protoc* 2021;**16**:1548−80.
24. Samuel M, Fonseka P, Sanwlani R, Gangoda L, Chee SH, Keerthikumar S, et al. Oral administration of bovine milk-derived extracellular vesicles induces senescence in the primary tumor but accelerates cancer metastasis. *Nat Commun* 2021;**12**:3950.
25. Hossain DMS, Javaid S, Cai M, Zhang C, Sawant A, Hinton M, et al. Dinaciclib induces immunogenic cell death and enhances anti-PD1-mediated tumor suppression. *J Clin Invest* 2018;**128**:644−54.
26. Wang YM, Ke J, Guo XM, Gou KJ, Sang ZT, Wang YB, et al. Chiral mesoporous silica nano-screws as an efficient biomimetic oral drug delivery platform through multiple topological mechanisms. *Acta Pharm Sin B* 2022;**12**:1432−46.
27. Zhou YH, Gao D, Wang YY, Liang L, Zhang QY, Han WW, et al. Worm-like micelles facilitate the intestinal mucus diffusion and drug accumulation for enhancing colorectal cancer therapy. *Chin Chem Lett* 2023:108967.
28. Qiu NS, Liu Y, Liu Q, Chen YZ, Shen LM, Hu MY, et al. Celastrol nanoemulsion induces immunogenicity and downregulates PD-L1 to boost abscopal effect in melanoma therapy. *Biomaterials* 2021;**269**:120604.
29. Chen WG, Sheng P, Chen YJ, Liang Y, Wu SX, Jia LY, et al. Hypoxia-responsive immunostimulatory nanomedicines synergize with checkpoint blockade immunotherapy for potentiating cancer immunotherapy. *Chem Eng J* 2023;**451**:138781.
30. Zhao M, Li J, Chen F, Han YY, Chen DW, Hu HY. Engineering nanoparticles boost TNBC therapy by CD24 blockade and mitochondrial dynamics regulation. *J Control Release* 2023;**355**:211−27.
31. Pfirschke C, Engblom C, Rickelt S, Cortez-Retamozo V, Garris C, Pucci F, et al. Immunogenic chemotherapy sensitizes tumors to checkpoint blockade therapy. *Immunity* 2016;**44**:343−54.
32. Garg AD, Martin S, Golab J, Agostinis P. Danger signalling during cancer cell death: origins, plasticity and regulation. *Cell Death Differ* 2014;**21**:26−38.
33. Kim KU, Kim WH, Jeong CH, Yi DY, Min H. More than nutrition: therapeutic potential of breast milk-derived exosomes in Cancer. *Int J Mol Sci* 2020;**21**:7327.
34. Li YT, Xing LY, Wang LL, Liu X, Wu LC, Ni MJ, et al. Milk-derived exosomes as a promising vehicle for oral delivery of hydrophilic biomacromolecule drugs. *Asian J Pharm Sci* 2023;**18**:100797.
35. Zhong J, Xia BZ, Shan SB, Zheng AP, Zhang SW, Chen J, et al. High-quality milk exosomes as oral drug delivery system. *Biomaterials* 2021;**277**:121126.
36. Munro S, Pelham HR. A C-terminal signal prevents secretion of luminal ER proteins. *Cell* 1987;**48**:899−907.
37. Wu Z, Newstead S, Biggin PC. The KDEL trafficking receptor exploits pH to tune the strength of an unusual short hydrogen bond. *Sci Rep* 2020;**10**:16903.

38. Wang G, Papasani MR, Cheguru P, Hrdlicka PJ, Hill RA. Gold-peptide nanoconjugate cellular uptake is modulated by serum proteins. *Nanomedicine* 2012;**8**:822−32.
39. Arakel EC, Schwappach B. Formation of COPI-coated vesicles at a glance. *J Cell Sci* 2018;**131**.
40. Sáenz JB, Sun WJ, Chang JW, Li J, Bursulaya B, Gray NS, et al. Golgicide A reveals essential roles for GBF1 in Golgi assembly and function. *Nat Chem Biol* 2009;**5**:157−65.
41. Qiu C, Han HH, Sun J, Zhang HT, Wei W, Cui SH, et al. Regulating intracellular fate of siRNA by endoplasmic reticulum membrane-decorated hybrid nanoplexes. *Nat Commun* 2019;**10**:2702.
42. Jiang XH, Wang N, Liu C, Zhuo Y, Liang L, Gan Y, et al. Oral delivery of nucleic acid therapeutics: challenges, strategies, and opportunities. *Drug Discov Today* 2023;**28**:103507.
43. Ott PA, Hodi FS, Robert C. CTLA-4 and PD-1/PD-L1 blockade: new immunotherapeutic modalities with durable clinical benefit in melanoma patients. *Clin Cancer Res* 2013;**19**:5300−9.
44. Champiat S, Dercle L, Ammari S, Massard C, Hollebecque A, Postel-Vinay S, et al. Hyperprogressive disease is a new pattern of progression in cancer patients treated by anti-PD-1/PD-L1. *Clin Cancer Res* 2017;**23**:1920−8.
45. Guan XW, Lin L, Chen J, Hu YY, Sun PJ, Tian HY, et al. Efficient PD-L1 gene silence promoted by hyaluronidase for cancer immunotherapy. *J Control Release* 2019;**293**:104−12.
46. Miao L, Li JJ, Liu Q, Feng R, Das M, Lin CM, et al. Transient and local expression of chemokine and immune checkpoint traps to treat pancreatic cancer. *ACS Nano* 2017;**11**:8690−706.
47. Gottfried E, Kreutz M, Mackensen A. Tumor-induced modulation of dendritic cell function. *Cytokine Growth Factor Rev* 2008;**19**:65−77.
48. Matsuda A, Patel T. Milk-derived extracellular vesicles for therapeutic delivery of small interfering RNAs. *Methods Mol Biol* 2018;**1740**:187−97.
49. Duran-Lobato M, Niu Z, Alonso MJ. Oral delivery of biologics for precision medicine. *Adv Mater* 2020;**32**:e1901935.
50. Lu L, Chen GX, Qiu YY, Li MW, Liu DH, Hu DH, et al. Nanoparticle-based oral delivery systems for colon targeting: principles and design strategies. *Sci Bull* 2016;**61**:670−81.
51. Wang J, Pan H, Li JY, Nie D, Zhuo Y, Lv YS, et al. Cell membrane-coated mesoporous silica nanorods overcome sequential drug delivery barriers against colorectal cancer. *Chin Chem Lett* 2023;**34**:107828.
52. Zhang YQ, Wang YY, Li X, Nie D, Liu C, Gan Y. Ligand-modified nanocarriers for oral drug delivery: challenges, rational design, and applications. *J Control Release* 2022;**352**:813−32.
53. Fan WW, Xia DN, Zhu QL, Li XY, He SF, Zhu CL, et al. Functional nanoparticles exploit the bile acid pathway to overcome multiple barriers of the intestinal epithelium for oral insulin delivery. *Biomaterials* 2018;**151**:13−23.
54. Kobayashi K, Qiao SW, Yoshida M, Baker K, Lencer WI, Blumberg RS. An FcRn-dependent role for anti-flagellin immunoglobulin G in pathogenesis of colitis in mice. *Gastroenterology* 2009;**137**:1746−17456 e1.
55. Larsen MT, Mandrup OA, Schelde KK, Luo Y, Sorensen KD, Dagnaes-Hansen F, et al. FcRn overexpression in human cancer drives albumin recycling and cell growth, a mechanistic basis for exploitation in targeted albumin-drug designs. *J Control Release* 2020;**322**:53−63.
56. Kim H, Jang H, Cho H, Choi J, Hwang KY, Choi Y, et al. Recent advances in exosome-based drug delivery for cancer therapy. *Cancers (Basel)* 2021;**13**:4435.
57. Song WT, Shen LM, Wang Y, Liu Q, Goodwin TJ, Li JJ, et al. Synergistic and low adverse effect cancer immunotherapy by immunogenic chemotherapy and locally expressed PD-L1 trap. *Nat Commun* 2018;**9**:2237.
58. Hartgers FC, Figdor CG, Adema GJ. Towards a molecular understanding of dendritic cell immunobiology. *Immunol Today* 2000;**21**:542−5.